The ATLAS[3D] project – II. Morphologies, kinemetric features and alignment between photometric and kinematic axes of early-type galaxies

Davor Krajnović,[1][*] Eric Emsellem,[1,2] Michele Cappellari,[3] Katherine Alatalo,[4] Leo Blitz,[4] Maxime Bois,[1,2] Frédéric Bournaud,[5] Martin Bureau,[3] Roger L. Davies,[3] Timothy A. Davis,[3] P. T. de Zeeuw,[1,6] Sadegh Khochfar,[7] Harald Kuntschner,[8] Pierre-Yves Lablanche,[1,2] Richard M. McDermid,[9] Raffaella Morganti,[10,11] Thorsten Naab,[12,13] Tom Oosterloo,[10,11] Marc Sarzi,[14] Nicholas Scott,[3] Paolo Serra,[10] Anne-Marie Weijmans[15][†] and Lisa M. Young[16][‡]

[1]*European Southern Observatory, Karl-Schwarzschild-Strasse 2, 85748 Garching bei München, Germany*
[2]*Université Lyon 1, Observatoire de Lyon, Centre de Recherche Astrophysique de Lyon and Ecole Normale Supérieure de Lyon, 9 avenue Charles André, F-69230 Saint-Genis Laval, France*
[3]*Sub-department of Astrophysics, University of Oxford, Denys Wilkinson Building, Keble Road, Oxford OX1 3RH*
[4]*Department of Astronomy and Radio Astronomy Laboratory, University of California, Berkeley, CA 94720, USA*
[5]*Laboratoire AIM Paris-Saclay, CEA/IRFU/SAp CNRS Université Paris Diderot, 91191 Gif-sur-Yvette Cedex, France*
[6]*Sterrewacht Leiden, Leiden University, Postbus 9513, 2300 RA Leiden, the Netherlands*
[7]*Max-Planck-Institute for Extraterrestrial Physics, Giessenbachstrasse, 85748 Garching, Germany*
[8]*Space Telescope European Coordinating Facility, European Southern Observatory, Karl-Schwarzschild-Strasse 2, 85748 Garching, Germany*
[9]*Gemini Observatory, Northern Operations Center, 670 N. A'ohoku Place, Hilo, HI 96720, USA*
[10]*ASTRON – Netherlands Institute for Radio Astronomy, Postbus 2, 7990 AA Dwingeloo, the Netherlands*
[11]*Kapteyn Astronomical Institute, University of Groningen, Postbus 800, 9700 AV Groningen, the Netherlands*
[12]*Max-Planck-Institute for Astrophysics, Karl-Schwarzschild-Strasse 1, 85741 Garching, Germany*
[13]*Universitäts-Sternwarte München, Scheinerstrasse 1, D-81679 München, Germany*
[14]*Centre for Astrophysics Research, University of Hertfordshire, Hatfield, Herts AL1 09AB*
[15]*Dunlap Institute for Astronomy & Astrophysics, University of Toronto, 50 St George Street, Toronto, ON M5S 3H4, Canada*
[16]*Physics Department, New Mexico Institute of Mining and Technology, Socorro, NM 87801, USA*

ABSTRACT

We use the ATLAS[3D] sample of 260 early-type galaxies to study the apparent kinematic misalignment angle, Ψ, defined as the angle between the photometric and kinematic major axes. We find that 71 per cent of nearby early-type galaxies are strictly aligned systems ($\Psi \leq 5°$), an additional 14 per cent have $5° < \Psi \leq 10°$ and 90 per cent of galaxies have $\Psi \leq 15°$. Taking into account measurement uncertainties, 90 per cent of galaxies can be considered aligned to better than $5°$, suggesting that only a small fraction of early-type galaxies ($\sim$10 per cent) are not consistent with the axisymmetry within the projected half-light radius. We identify morphological features such as bars and rings (30 per cent), dust structures (16 per cent), blue nuclear colours (6 per cent) and evidence of interactions (8 per cent) visible on ATLAS[3D] galaxies. We use KINEMETRY to analyse the mean velocity maps and separate galaxies into two broad types of regular and non-regular rotators. We find 82 per cent of regular rotators and 17 per cent of non-regular rotators, with two galaxies that we were not able to classify due to the poor data quality. The non-regular rotators are typically found in dense regions and are massive. We characterize the specific features in the mean velocity and velocity dispersion maps. The majority of galaxies do not have any specific features, but we highlight here the frequency of the kinematically distinct cores (7 per cent of galaxies) and the aligned double

[*]E-mail: dkrajnov@eso.org
[†]Dunlap Fellow.
[‡]Adjunct Astronomer with the National Radio Astronomy Observatory.

peaks in the velocity dispersion maps (4 per cent of galaxies). We separate galaxies into five kinematic groups based on the kinemetric features, which are then used to interpret the ($\Psi-\epsilon$) diagram. Most of the galaxies that are misaligned have complex kinematics and are non-regular rotators. In addition, some show evidence of the interaction and might not be in equilibrium, while some are barred. While the trends are weak, there is a tendency that large values of Ψ are found in galaxies at intermediate environmental densities and among the most massive galaxies in the sample. Taking into account the kinematic alignment and the kinemetric analysis, the majority of early-type galaxies have velocity maps more similar to that of the spiral discs than to that of the remnants of equal-mass mergers. We suggest that the most common formation mechanism for early-type galaxies preserves the axisymmetry of the disc progenitors and their general kinematic properties. Less commonly, the formation process results in a triaxial galaxy with much lower net angular momentum.

Key words: galaxies: elliptical and lenticular, cD – galaxies: formation – galaxies: kinematics and dynamics.

1 INTRODUCTION

The internal dynamics of early-type galaxies hold important clues about their formation. Looking at their morphological structure alone, early-type galaxies appear to be simple and uniform, but increasingly better observational technology and methods have revealed much more complex systems rich in internal dynamics and substructures. Crucial for this were the kinematic observations of early-type galaxies (Illingworth 1977; Davies et al. 1983; Davies & Illingworth 1983; Bender 1988b; Bender & Nieto 1990) and two significant discoveries that some ellipticals rotate slowly (Bertola & Capaccioli 1975; Illingworth 1977) and that there are objects with significant rotation around the major-axis (Davies & Birkinshaw 1986, 1988; Franx, Illingworth & Heckman 1989; Jedrzejewski & Schechter 1989). This showed that among early-type galaxies there are systems with triaxial figures, perhaps even slowly tumbling (Schwarzschild 1982; van Albada, Kotanyi & Schwarzschild 1982), and their internal structure is not determined by their total mass and angular momentum alone (see the review by de Zeeuw & Franx 1991).

Although discoveries of galaxies with the rotation around the long axis were very exciting, the majority of galaxies seemed to show the rotation around the apparent minor-axis (Schechter & Gunn 1979; Efstathiou, Ellis & Carter 1980; Davies et al. 1983; Dressler & Sandage 1983; Bender 1988a; Davies & Birkinshaw 1988; Franx et al. 1989; Jedrzejewski & Schechter 1989; Bender & Nieto 1990; Bender, Saglia & Gerhard 1994). Over the decade preceding the late 1990s, a picture emerged of elliptical galaxies exhibiting a range of properties with luminous objects having slow rotation, anisotropic velocity distributions, boxy isophotes and cores, taken to be indicative of triaxial figures, and less-luminous galaxies having shapes flattened by the rotation, isotropic velocity distributions, discy isophotes and cuspy cores, taken to be indicative of oblate figures (for a synthesis, see Kormendy & Bender 1996).

The most straightforward evidence for the triaxiality is the observation of a misalignment between the galaxy's angular momentum vector and the minor-axis. In axisymmetric galaxies, these two axes are aligned. Stationary triaxial shapes support four major types of regular stellar orbits: box orbits, short-axis tubes, and inner and outer long-axis tubes (de Zeeuw 1985). Given that among the tubes it is also possible to have both prograde and retrograde orbits, the combination of these major families will result in the total angular momentum vector pointing anywhere in the plane containing both the long axis and the short axis of the system (e.g. Statler 1987). Furthermore, it is also possible to have a radial variation of the relative weights assigned to different orbital families which will give rise to radially different kinematic structures and contribute to the radial variation of the observed misalignment (see van den Bosch et al. 2008, for a detailed orbital analysis of a triaxial system).

In addition to the orbital origin of the misalignment between the shape of the system and its internal kinematics, it is also possible to observe a misalignment from pure projection effects, given that the orientation of a triaxial galaxy towards an observer is random. Hence, the angle at which the apparent minor-axis of the observed (projected on the sky) galaxy is seen will be different from the angle of the projected short axis of the galaxy (Contopoulos 1956; Stark 1977; Kondratev & Ozernoi 1979). When this is combined with a projection of the angular momentum vector, which depends on the specific orbital structure, we expect that the misalignment between the angular momentum vector and the principal axis will be observed regularly. This was beautifully illustrated by Statler (1991) with the montage of velocity maps of a triaxial model viewed at different projection angles.

The combination of the apparent orientation of the total angular momentum and the apparent shape of the system can be used to statistically constrain the intrinsic shape of early-type galaxies as a family of objects, including the case when the figure rotation is present (Binney 1985). The first analysis of the apparent misalignment angle, defined as $\tan \Psi = v_{min}/v_{maj}$, where v_{min} and v_{maj} are velocity amplitudes along the minor-axis and major-axis, respectively, was presented by Franx, Illingworth & de Zeeuw (1991). They compiled from the existing literature all galaxies for which it was possible to estimate Ψ reasonably well and obtain their ellipticities. This compilation confirmed that the majority of early-type galaxies indeed had small misalignments, with a few cases showing the long-axis rotation [rotation around the major (long) axis]. In terms of the intrinsic shape of early-type galaxies, their results showed a wide range of acceptable solutions including distributions of only nearly oblate shapes, oblate and prolate shapes, as well as purely triaxial shapes.

The SAURON survey (de Zeeuw et al. 2002) provided velocity maps reaching to about one effective radius for a sample of nearby early-type galaxies. The survey confirmed the main findings of the previous decades and established that many of the dynamical properties of early-type galaxies are related to a measure of their

specific angular momentum, which was available for the first time from velocity and velocity dispersion maps (Emsellem et al. 2004). Based on their apparent angular momentum, the early-type galaxies separate into slow and fast rotators (Emsellem et al. 2007), where slow rotators are weakly triaxial, but not far from isotropic, while fast rotators are nearly axisymmetric, intrinsically flatter and span a large range of anisotropies (Cappellari et al. 2007). Furthermore, the fast rotators are aligned, while slow rotators are misaligned (Emsellem et al. 2004; Cappellari et al. 2007). This global property is followed locally where fast rotators do not show radial changes in the orientation of the velocity maps, which is, however, typical for slow rotators (Krajnović et al. 2008).

In addition, the SAURON velocity maps of slow rotators exhibit a variety of kinematic structures, such as kinematic twists, kinematically distinct cores or showing no rotation at all, while the velocity maps of fast rotators are kinematically more uniform showing disc-like kinematics (Krajnović et al. 2008). This suggests that the difference in the appearance of the velocity maps of these two types of galaxies is related to their internal structures and is a consequence of their (different) evolution paths. The features visible in the kinematic maps are the end-products of various processes and it is potentially useful to assess their relative importance.

The SAURON survey found 25 per cent of slow rotators among the nearby early-type galaxies. The SAURON sample, however, is not representative of the luminosity function of early-type galaxies and a question remains: what is the relative fraction of galaxies consistent with being axisymmetric? This question is relevant for our understanding of the importance of the gas dissipation in the formation of early-type galaxies via the hierarchical merging. Collisionless mergers of roughly equal mass progenitors generally produce triaxial galaxies, while the gas dissipation generates nearly axisymmetric systems with discs (e.g. Naab, Jesseit & Burkert 2006; Jesseit et al. 2007; Hoffman et al. 2009). Observations of the molecular, atomic and ionized gas (Oosterloo et al. 2002; Morganti et al. 2006; Sarzi et al. 2006; Serra et al. 2008; Young, Bureau & Cappellari 2008; Crocker et al. 2009; Oosterloo et al. 2010) suggest that the evolution of early-type galaxies is significantly influenced by gas reservoirs, both free or bound to other galactic systems. The presence of the gas inevitably results in the dissipation playing a major role in the evolution.

The purpose of this work is three-fold: (i) to analyse the kinematic maps and images of the volume-limited sample of nearby early-type galaxies gathered by the ATLAS^{3D} project (Cappellari et al. 2011a, hereinafter Paper I); (ii) to characterize quantitatively the morphological and kinematic features and determine their frequency; and (iii) to measure the kinematic misalignment angle by exploiting the completeness of the sample and the two-dimensional coverage of the kinematic data. Specifically, we explore the connection between the kinematic misalignment, the morphology and kinematic structures of nearby early-type galaxies. In this respect, this paper follows Paper I and its main results are used in Emsellem et al. (2011, hereinafter Paper III).

In Section 2, we briefly describe the ATLAS^{3D} sample and the types of data used in this paper. In Section 3, we characterize the morphological and kinematical structures observed in the sample with more emphasis given to the latter. We separate early-type galaxies based on their rotation, define various features visible in the kinematic maps and identify galaxies according to these properties. This is followed by definitions of kinematic and photometric position angles (PAs), and the description of how these, as well as the ellipticity of the galaxies, were measured together with an estimate of the uncertainty (Section 4). The distribution of the kinematic misalignment angle is shown in Section 5, which is followed by a discussion (Section 6) and conclusions (Section 7).

2 SAMPLE AND OBSERVATIONS

The ATLAS^{3D} sample and its selection is described in detail in Paper I. Here, we briefly outline the main properties. Our galaxies were selected from a parent sample of objects brighter than $M_{K_s} < -21.5$ mag and a local volume with a radius of $D = 42$ Mpc using the observability criterion that the objects have to be visible from the William Herschel Telescope (WHT) on La Palma: $|\delta - 29°| < 35°$, where δ is the sky declination, excluding the dusty region near the Galaxy equatorial plane. Galaxies were selected using the 2MASS Extended Source Catalog (Jarrett et al. 2000), while the classification of early-type galaxies was based on the visual inspection of the available imaging: SDSS and DSS colour images. Here the main selection criterion was the lack of spiral arms or dust lanes in highly inclined galaxies, following the Hubble classification (Hubble 1936; de Vaucouleurs et al. 1991) as outlined in Sandage (1961). The final sample contains 260 nearby early-type galaxies.

Kinematic data used in this study were obtained using the SAURON integral-field spectrograph (IFS; Bacon et al. 2001) mounted on the WHT. SAURON is an IFS with a field-of-view (FoV) of 33×41 arcsec^2. The observing strategy and the data reduction are also described in detail in Paper I. The SAURON FoV, or mosaics of two SAURON pointings, was oriented along the major-axis of the galaxies such as to maximize the coverage. Typically, maps encompass one effective radius, although for the largest galaxies, only half of the effective radius is fully covered (see Paper III). The data reduction follows procedures described in Bacon et al. (2001) and Emsellem et al. (2004). For 212 galaxies we used publicly available SDSS Data Release 7 r-band images (Abazajian et al. 2009). For galaxies which were not observed by the SDSS, we had imaging campaigns using the Wide Field Camera on the Isaac Newton Telescope on La Palma, also in the r band. There we observed 46 galaxies and the data reduction and calibrations are presented in Scott et al. (in preparation). Finally, there were two galaxies for which we were not able to obtain r-band images and in this study we used Two-Micron All-Sky Survey (2MASS) K-band observations instead.

3 CHARACTERIZATION OF MORPHOLOGICAL AND KINEMATIC STRUCTURES IN THE ATLAS^{3D} SAMPLE

In this section, we describe morphological and kinematic features found in ATLAS^{3D} galaxies. We are primarily interested in highlighting the existence of bars, rings, shells or other interaction features, as well as the existence of dusty discs or filamentary structures in the images. We also analyse the mean-velocity maps and describe the kinematic features and their frequency in our sample. We point out the most significant features and accordingly sort galaxies in five kinematic groups which will be used in the rest of this paper. Additional remarks, images of velocity maps of the full sample and a table with the morphological and kinematic characteristics of galaxies are presented in Appendices A, C and D, respectively.

3.1 Morphological features

Our morphological characterization is purely visual, based on SDSS and INT r-band images as well as the SDSS true colour (red–green–blue) images (Lupton et al. 2004) when available, but we do not

Table 1. A summary of morphological features in ATLAS^{3D} galaxies.

Feature (1)	Number (2)	Dust disc (3)	Filaments (4)	Blue features (5)
N	159	18 [16]	8 [7]	7 [4]
B	35	2 [1]	1 [0]	2 [0]
R	13	3 [2]	1 [0]	2 [0]
BR	30	1 [1]	3 [1]	2 [0]
S	9	0 [0]	1 [0]	1 [0]
I	12	0 [0]	6 [5]	1 [0]

Notes. The total number of galaxies is 260; morphological and dust features were not classified in two galaxies without SDSS or INT imaging. Column (1): morphological features: N – no feature, regular shape; B – bar; R – ring; BR – bar and ring; S – shells; and I – any other evidence for interaction. Column (2): number of galaxies with morphological features in Column (1). Column (3): galaxies with dust discs. Column (4): galaxies with dust filaments. Column (5): galaxies with blue colour features. Columns (3–5): within brackets is the number of only those galaxies that have the features listed in that column (a dusty disc, dusty filaments or a blue feature).

attempt to quantify the amount of dust, the structure of shells or tidal tails, or the properties of bars. Our goal is to measure the frequency of obvious structures as they are visible in our *r*-band images. Occasionally, for confirmation of not clearly recognizable bars, we also use the information contained in absorption and emission-line maps. A summary of morphological features found in ATLAS^{3D} galaxies is given in Table 1, while the SDSS and INT colour images of the galaxies are shown in Paper I.

Bars are detected in ∼25 per cent of the galaxies in our sample (65 galaxies), while rings are seen in ∼17 per cent of the sample (43 galaxies). Rings and bars often occur together, and about half of the barred systems have clearly visible rings, but there are 13 ringed systems with no obvious bar-like structure. The rings in these systems resemble resonance rings (they do not appear as polar or collisional rings). There are three cases of dusty and blue, possibly star-forming, rings (NGC 3626, 4324 and 5582). The total fraction of galaxies with bars and/or rings increases to 30 per cent (78 galaxies). This is still likely a lower limit, but if we consider only galaxies with the de Vaucouleurs type between −3 and 0 (175 galaxies in the ATLAS^{3D} sample), 45 per cent of galaxies have bars/rings in our sample. This is in excellent agreement with a recent near-infrared survey of barred S0 galaxies (Laurikainen et al. 2009).

We looked for dust using the same *r*-band SDSS and INT images. We found 24 systems with dust in ordered discs and 20 systems with filamentary dusty features, giving the total fraction of dusty systems of 18 per cent. An inspection of colour images reveals 15 galaxies (6 per cent) with some evidence of blue colours, half of which are found in the nuclei and half in (circumnuclear) rings. Here we report the obvious cases and their number is likely a lower limit only, but this does not influence the results of this paper. Note there are some well-known cases of nuclear dust discs visible from space-based observations (e.g. NGC 4261, Jaffe et al. 1996), which we do not see in our ground-based images. We do not include them in our statistics. Similarly, we do not look for other morphological features below the spatial resolution of our images (e.g. nuclear bars).

The evidence for the past interaction of various degrees is seen in 21 (8 per cent) galaxies (based on our images from the SDSS and INT). These objects are likely at different stages of interaction, but they are mostly not actively merging systems. In particular, shells are visible in nine systems at our limiting surface brightness of ∼26 mag arcsec^{-2}. The evidence of past interactions is visible

at all environmental densities, but they do not occur in galaxies which have other morphological perturbations (such as bars) at our surface brightness limit. In most cases, the interacting galaxies do not show ordered dusty discs in the central regions. Filamentary dust features, however, can be found in half of the interacting galaxies. A specific study of shells and other interaction features based on deeper MegaCam images will be a topic of a future paper in the series.

3.2 Kinematic structures

The majority of velocity maps of early-type galaxies in our sample show ordered rotation. More complex features, although present, are not common. We use the mean velocity and the velocity dispersion maps to perform a complete description of kinematic structures that occur in the early-type galaxies of our volume-limited sample.

3.2.1 Two types of rotation

We performed an analysis similar to Krajnović et al. (2008) using KINEMETRY[1] (Krajnović et al. 2006) on velocity maps. This method consists of finding the best-fitting ellipse along which the velocities can be described as a function of a cosine change in the eccentric anomaly. In that respect, KINEMETRY is a generalization of the isophotometry of surface brightness images (Carter 1978; Lauer 1985; Bender & Moellenhoff 1987; Jedrzejewski 1987) to other moments of the line-of-sight velocity distribution (LOSVD) (the mean velocity, velocity dispersion, etc.). This means that the stellar motions along this ellipse can be parametrized by a simple law, $V = V_{\rm rot} \cos(\theta)$, where $V_{\rm rot}$ is the amplitude of rotation and θ is the eccentric anomaly. Note that the same expression describes the motion of gas clouds on circular orbits in a thin (inclined) disc (e.g. Schoenmakers, Franx & de Zeeuw 1997; Wong, Blitz & Bosma 2004) and that, when KINEMETRY is applied to the velocity maps of thin gas discs, it achieves similar results to the titled-ring method (e.g. Begeman 1987; Staveley-Smith et al. 1990; Franx, van Gorkom & de Zeeuw 1994). There are, however, conceptual differences. The tilted-ring method determines the best-fitting ellipse by fitting a cosine function in a least-squares sense along an elliptical path, whereas KINEMETRY performs a rigorous generalization of the photometric ellipse fitting. It determines the best-fitting ellipse by minimizing the Fourier coefficients up to the third, except the $\cos(\theta)$, term. This ensures a more robust fit and ensures that the higher order Fourier terms are unaffected by the ellipse fit. Moreover, the approach adopted by KINEMETRY allows the same method to be used to fit both photometric and kinematic data. The method first fits for the ellipse parameters, PA, $\Gamma_{\rm kin}$ and flattening of the ellipse $q_{\rm kin}$. The velocity profile along the best-fitting ellipse is then decomposed into odd Fourier harmonics. The first-order k_1 is equivalent to $V_{\rm rot}$, while the higher order terms show departures of the velocity profiles from the assumed cosine law. Examples of typical kinematic radial profiles of the 48 early-type galaxies from the SAURON survey, most of which are also part of the ATLAS^{3D} sample, can be found in appendix B of Krajnović et al. (2008), while examples of residual velocity maps obtained by subtracting KINEMETRY fits are given in Krajnović et al. (2006).

Deviations from the cosine law can be quantified by measuring the amplitude of the k_5 harmonics. In practice, it is better to use a

---

[1] The IDL KINEMETRY routine can be found at http://www.eso.org/~dkrajnov/idl

scale-free measure which is given by dividing k_5 with local rotation k_1. In order to characterize each object, we use the radial profiles to calculate the luminosity-weighted average ratio $\overline{k_5/k_1}$, following the prescription from Ryden et al. (1999). We exclude rings for which KINEMETRY was not able to find a good fit (i.e. the ellipse flattening hits the boundary value). We estimate the uncertainty on $\overline{k_5/k_1}$ with a Monte Carlo approach by perturbing each point of the k_5/k_1 radial profile based on its measurement error, calculate the luminosity-weighted average and repeat the process 1000 times. The uncertainty is the standard deviation of the Monte Carlo realizations. The values of $\overline{k_5/k_1}$ are determined within one effective radius or within the semimajor-axis radius of the largest best-fitting ellipse that is enclosed by the velocity map.

We set a limit of $\overline{k_5/k_1} < 0.04$ for the velocity map to be well described by the cosine law. The choice for this number is somewhat arbitrary, but we based it on the mean uncertainty on k_5/k_1 for all galaxies ($\sim$0.03) and the resistant estimate of its dispersion ($\sim$0.01). Note that this is higher than the 2 per cent used by Krajnović et al. (2008), but the observations of the SAURON sample were of higher signal-to-noise ratios and lower average uncertainty on k_5/k_1 (0.015). If $\overline{k_5/k_1}$ is larger than 4 per cent, we flag the velocity map as not being consistent with the cosine law. In this way, we separate two types of rotations among early-type galaxies.

Galaxies of the first type, consistent with having $\overline{k_5/k_1} < 0.04$, have velocity maps dominated by ordered rotation. These we call *regular rotators* (RRs). Galaxies of the second type, consistent with $\overline{k_5/k_1} > 0.04$, have velocity maps characterized by more complex structures, including cases where the rotation is not detectable. As a contrast to the RR galaxies, we call them *non-regular rotators* (NRRs). The majority of objects in the ATLAS[3D] sample belong to the RR type (214 or 82 per cent), while there are 44 (17 per cent) objects of the NRR type. We were not able to classify two galaxies (PGC 058114 and PGC 170172) due to the low signal-to-noise ratio and an unfortunate position of a bright star.

3.2.2 Kinematic features

The majority of the velocity maps are dominated by ordered rotation, but there are several distinct features recognizable in the kinematic maps, especially among the galaxies of the NRR type. The diversity of the kinematic features suggests a variety of formation processes at work in early-type galaxies. We wish to describe these fossil records and quantify their frequency among the two rotation types. As above, we use the KINEMETRY analysis within one effective radius (or within the semimajor-axis radius of the largest best-fitting ellipse that is enclosed by the velocity map) to define various kinematic features occurring in our sample:

(i) *No-feature* (NF) velocity maps are flagged if the orientation of the best-fitting ellipses, Γ_{kin}, is constant with the radius (for both the RR and the NRR types of rotation). In the case of NRR galaxies with a measurable rotation, Γ_{kin} can also change erratically between adjacent rings.

(ii) *Double maxima* (2M) have radial profiles of the k_1 parameter characterized by a rapid rise in the velocity reaching a maximum value, which is followed by a decrease and subsequent additional rise to a usually larger velocity. These velocity maxima are aligned.

(iii) *Kinematic twist* (KT) is defined as a smooth variation in Γ_{kin} with an amplitude of at least $10°$ over the map.

Table 2. A summary of kinematric types and features in the ATLAS[3D] sample.

Feature	RR	NRR	Comment
NF	171	12	No feature on the map
2M	36	0	Double maxima in the radial velocity profile
KT	2	0	Kinematic twist
KDC	0	11	Kinematically distinct core
CRC	1	7	Counter-rotating core
2σ	4	7	Double peak on a σ map
LV	0	7	Low-level velocity (non-rotator)

Notes. The total number of galaxies is 260 and two galaxies were left unclassified in terms of their kinematic features.

(iv) *Kinematically distinct core* (KDC)[2] is defined when there is an abrupt change in Γ_{kin} with a difference larger than $30°$ between adjacent components and k_1 drops to zero in the transition region. We require that at least two consecutive rings have a similar Γ_{kin} measurement within the component.

(v) *Counter-rotating core* (CRC) is a special case of the KDC where the change in Γ_{kin} is of the order of $180°$.

(vi) *Low-level velocity* (LV) map is defined when $k_1 < 5\,\mathrm{km\,s^{-1}}$. In these cases, the rotation is not measurable and KINEMETRY cannot determine the ellipse parameters.

(vii) *Double σ* (2σ) feature is found by visually inspecting the velocity dispersion maps. This feature is characterized by two off-centre, but symmetric, peaks in the velocity dispersion, which lie on the major-axis of the galaxy. We require that the distance between the peaks in the velocity dispersion map is at least half the effective radius.

In principle, each map could be characterized by a combination of a few of the above features. Specifically, all features could occur both in RR and in NRR galaxies, but this is generally not the case, as it can be seen in Table 2, which summarizes the kinematric features found in the ATLAS[3D] sample. This can be understood by considering that any feature in the velocity map, especially those associated with the change in Γ_{kin}, will disturb the map such that k_5/k_1 will increase. Unless those features are small (relative to $1R_e$), $\overline{k_5/k_1}$ will be larger than 4 per cent and, hence, the galaxy will be classified as a NRR. An exception is the 2M feature since the two maxima are aligned and k_5/k_1 might increase only within the region of the rotation dip (see Krajnović et al. 2006 for examples of the model velocity maps and their analysis). For a discussion on the differences between 2M, KDC, 2σ and CRC galaxies, see Appendix B.

As stated above, the majority of galaxies are of the RR type and they do not have any specific feature (66 per cent). The second most-common feature (14 per cent) is the aligned maxima in the velocity maps (2M) and they occur only in the RR type. In a few cases, RR-type galaxies are also found to show KT (two), CRC (one) and 2σ (three) features. The mean-velocity maps of these more complex kinematic features are typically only marginally consistent with being of the RR type.

A number of galaxies with different features are evenly spread among the NRR type. There are 18 (7 per cent) galaxies that have

---

[2] There is some confusion in the literature on the naming of these kinematic structures. Both decoupled/distinct and core/component terms are used to specify the same thing. We choose to use the combination of distinct cores in order to stress that they happen in the central regions of the galaxies but they might not be dynamically decoupled from the rest of the system.
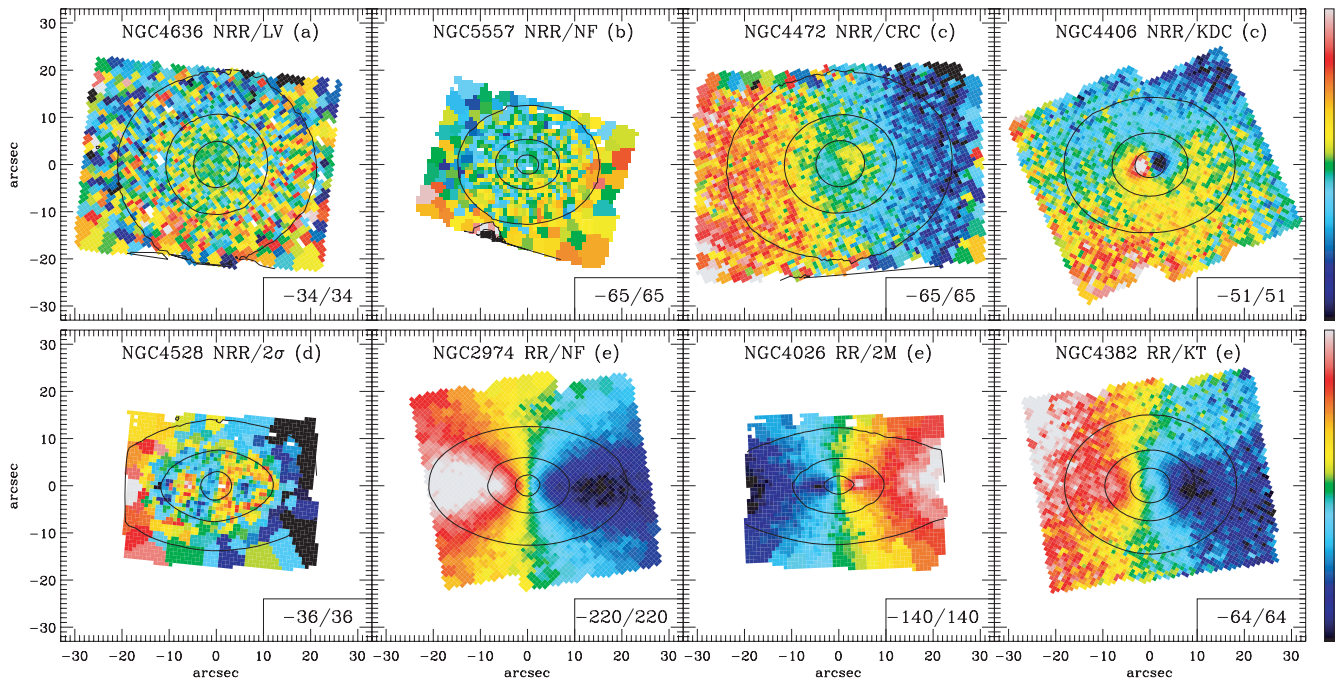
Figure 1. Example of various features found on the mean velocity maps of ATLAS[3D] galaxies. From the left-hand to right-hand side (top to bottom): NRR/LV (NGC 4636) part of group a, NRR/NF (NGC 5557) part of group b, NRR/CRC (NGC 4472) and NRR/KDC (NGC 4406) part of group c, NRR/2σ (NGC 4528) part of group d, and representing group e are RR/NF (NGC 2974), RR/2M (NGC 4026) and RR/KT (NGC 4382). All maps are oriented such that the large-scale photometric major-axis is horizontal. Values in the lower right-hand corners show the range of the plotted velocities in km s^{-1}. For the definition of the kinematic groups, see Table 3.

a KDC or a CRC feature (11 and seven objects, respectively), 12 (~5 per cent) do not show any features, seven (~3 per cent) do not have any detectable rotation, while seven have 2σ peaks on velocity dispersion maps. It is possible that about a third of NRR/NF maps would be classified as RR/NF in lower noise velocity maps. Possible candidates include NGC 770, 4690, 5500 and 5576. In Fig. 1, we show examples of the velocity maps dominated by the typical kinemetric features.

3.2.3 Five kinematic groups of early-type galaxies

In Section 3.2.1, we quantified two types of rotation present in early-type galaxies, while in Section 3.2.2, we discussed all features visible on kinematic maps in our sample. In Paper III, we separate galaxies according to their specific (projected) angular momentum into fast and slow rotators. That separation is somewhat arbitrary and we use the two types of rotations in the velocity maps (RR and NRR) to empirically divide slow and fast rotators. In the rest of this paper, we will continue to use the terminology of the RR and NRR type of rotation, instead of fast and slow rotators, but we emphasize the respective similarity between these definitions, although it is not a priori necessary that all RR galaxies are FR galaxies (see Paper III).

The majority of galaxies are RR galaxies without specific features, while a minority of galaxies show a variety of kinematic substructures. The fact that certain features do not occur in one of the two types of rotation presents a constraint on the galaxy formation. In order to facilitate the usefulness of these features, we propose a system of five groups, which is based on the reduction of non-occurring features and blending of features with likely similar origin.

Table 3. Kinematic groups.

Group	Number of galaxies	Feature
a	7	NRR/LV
b	12	NRR/NF
c	19	NRR/KDC, NRR/CRC, RR/CRC
d	11	NRR/2σ, RR/2σ
e	209	RR/NF, RR/2M, RR/KT
f	2	U

Notes. The last row is reserved for galaxies for which we were not able to determine kinematic features and which remain *unclassified*.

In Table 3, we summarize the five groups. Note that in Table 3 we used only features which occur in our sample, but the intention is that *group a* consists of galaxies which do not show any rotation, while *group b* consists of galaxies with complex velocity maps, but which do not show any specific feature. *Group c* comprises kinematically distinct cores, including the subgroup of CRCs, while *group d* has galaxies with double peaks in the velocity dispersion maps. The most numerous is *group e*, consisting of galaxies with simple rotation and of galaxies with two aligned velocity maxima or with minor KTs. In Fig. 1, we link the typical kinematic features with the five significant kinematic groups.

The three pie-chart diagrams in Fig. 2 visualize the frequency of the two types of rotation, different kinemetric features and their inclusion to significant kinematic groups. As mentioned before, the majority of early-type galaxies in the local Universe are ordered, RRs. There are, however, a number of different kinemetric features visible in the maps of the mean velocity and velocity dispersion, but they mostly occur in NRRs. Finally, the last diagram shows the relative frequency of the five most significant kinematic groups in
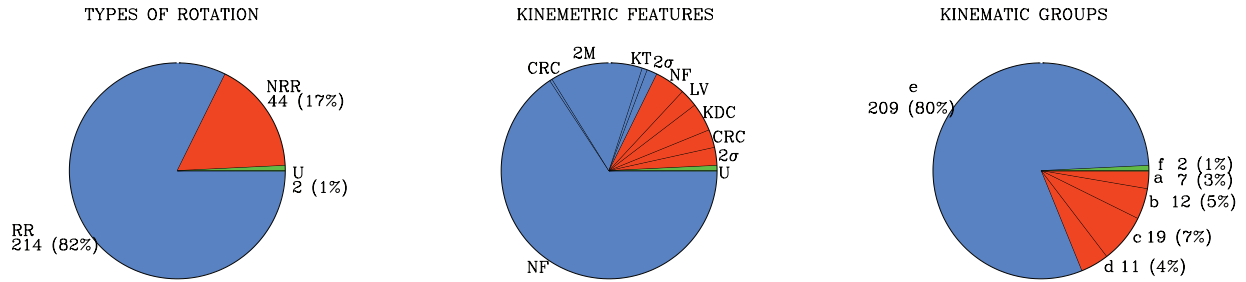
Figure 2. Diagrams presenting the kinematic analysis of ATLAS^{3D} galaxies. Left-hand diagram: the frequency of two types of rotators: RRs and NRRs. Middle diagram: the kinematric features. Only those features found in our sample are shown. The numbers of galaxies are not shown for clarity. They are given in Table 2. Right-hand diagram: the five kinematic groups comprising significant kinemetric features. Letters a–f are explained in Table 3. In all diagrams, the blue colour refers to ordered velocity maps that can be described by the cosine law ($\overline{k_5/k_1} \leq 0.04$) and the red colour refers to the complex velocity maps poorly described by the cosine law ($\overline{k_5/k_1} > 0.04$). Objects which were not classified are represented by the green slice and marked with 'U'.

the ATLAS^{3D} sample. Note that the number of e galaxies (209) is not equal to the number of RR systems (214). The reason is that that one RR/CRC and four RR/2σ galaxies were put together with other NRR/CRC and NRR/2σ systems into groups c and d.

For a discussion on possible caveats of the kinemetric analysis, we refer the reader to Appendix A, while in Appendix C we show the velocity maps of all ATLAS^{3D} galaxies sorted in their kinematic groups.

3.2.4 Linking morphology, kinematics and environment

Fig. 3 shows a histogram of morphological features of ATLAS^{3D} galaxies. We created four bins grouping objects with resonance phenomena (including bars, rings and bars with rings), interaction features (including shells and other interaction characteristics), dust/blue (including filamentary dust, dust discs and the blue nuclear colours) and featureless galaxies with the regular early-type morphology. In the same histogram, we added the frequency of galaxies of the five kinematic groups for a given morphological fea-
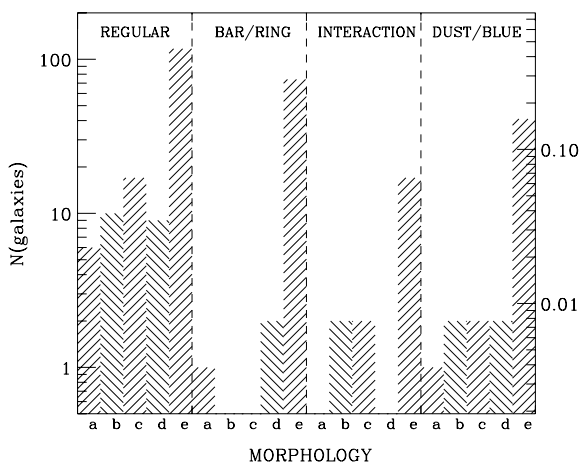

Figure 3. Histogram with the comparison of morphological and kinematic features in ATLAS^{3D} galaxies. The morphological features are binned into *regular* (featureless and regular shapes), *bar/ring* (bars and/or rings), *interaction* (shells or other interaction features) and *dust/blue* (dusty filaments, dusty discs or blue nuclear features). The hatched vertical bars show the number of galaxies having that morphological feature and being part of one of the five kinematic groups (a, b, c, d and e). The right-hand axis is in units of the total number of galaxies in the sample.

ture. It is hardly surprising that in all morphological bins the most represented are the galaxies of group e (RR galaxies), given that this is also the most numerous group.

It is somewhat surprising that galaxies with evidence for interaction do not show more complex kinematics (only two galaxies are from groups b and c), which is probably due to the difference in the dynamical state and time-scales between the large (interaction features) and small scales (kinematics). The resonance phenomena are linked to disc-dominated systems and almost all galaxies in this bin show regular velocities. There are three exceptions of which one deserves special attention: a barred NRR/LV (NGC 4733), which is seen at very low inclination and, hence, likely an object with the intrinsic rotation. Dust or blue nuclear features are also present in galaxies of all groups with complex kinematics, but only in one or two galaxies per group. In this group, there is also a special case: a round NRR/LV galaxy (NGC 3073) which also has blue ultraviolet colours (Donas et al. 2007).

Complex kinemetric features (groups a, b, c and d) are mostly found in galaxies with typical, featureless, early-type morphologies, confirming the reputation of early types that while looking simple, they retain complex internal structure. All intrinsically non-rotating galaxies (group a) are here, as well as the majority of galaxies with KDCs or just complex velocity maps. Galaxies with two peaks in the velocity dispersion maps are also mostly found in this bin. This suggests that any process that shaped these galaxies has happened a long time ago.

As an illustration of the environmental influence on the kinematics of galaxies (and the membership to a specific kinematic group), we show in Fig. 4 the distribution on the sky of all galaxies brighter than -21.5 mag in the K band of the parent sample (Paper I; both ATLAS^{3D} and spiral galaxies). The kinematic groups are distinguished by different symbols. The top panel shows the Northern hemisphere and, excluding the Virgo cluster, it can be seen that the spirals and galaxies from group e have a relatively similar spatial distribution, while the galaxies with complex kinematics are found typically surrounded, in projection, by other galaxies. Obvious exemptions are two group a galaxies in the northern part of the plot: NGC 3073 (RA $\sim$ 150°) and NGC 6703 (RA $\sim$ 280°). Three other galaxies are in less densely populated regions: NGC 5557 from group b [right ascension (RA) $\sim$ 210°], NGC 661 from group c (RA $\sim$ 25°) and NGC 448 from group d (RA $\sim$ 20°). For NGC 3073 and 6703, there is evidence that they are actually discs seen at low inclinations (de Vaucouleurs et al. 1991; Paper III), while both NGC 448 and 661 have 2σ peaks in their velocity dispersion maps, but the separation between the peaks for NGC 661 is
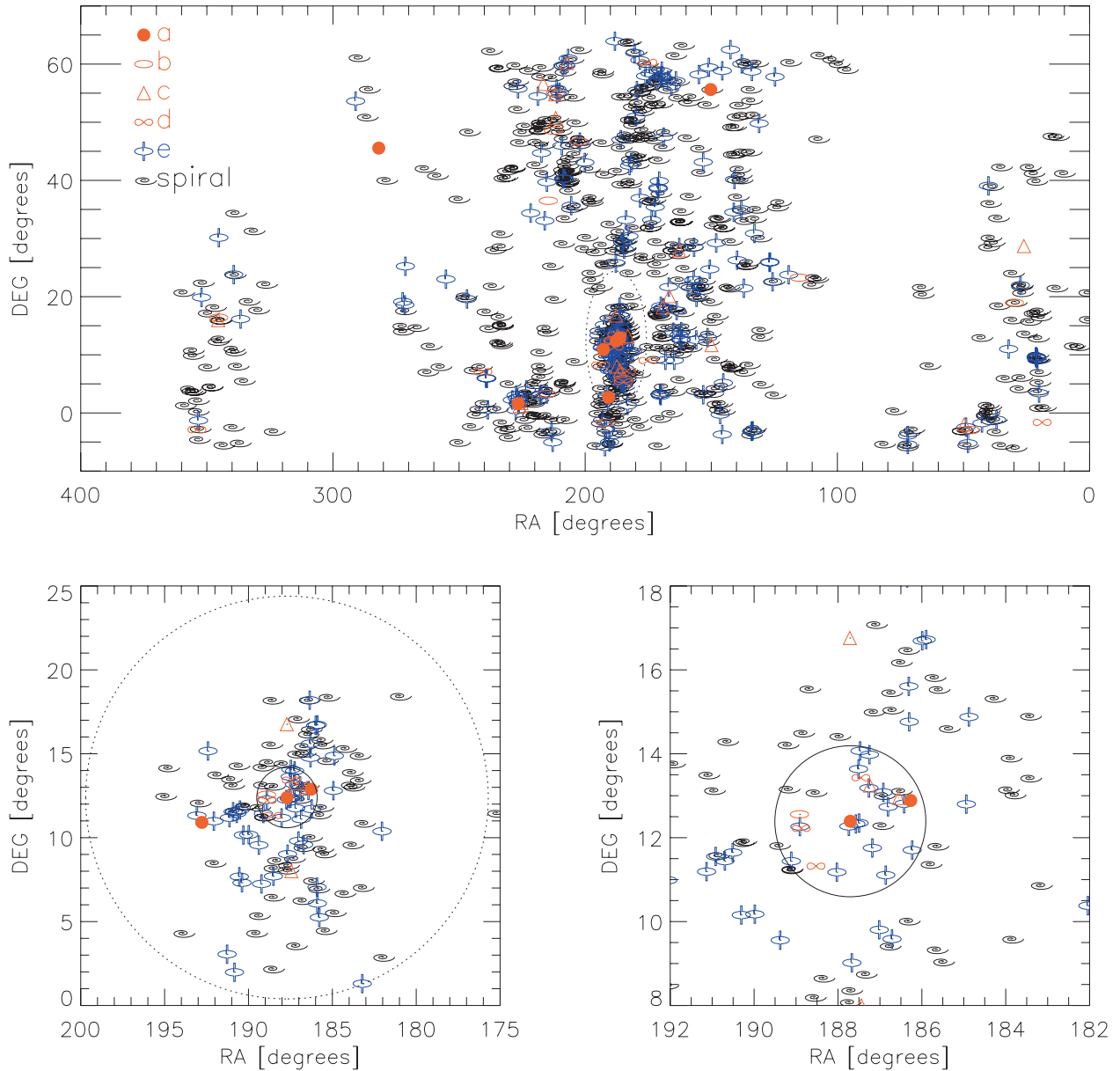
Figure 4. The spatial distribution of kinematic groups of ATLAS^{3D} galaxies. All galaxies with $M_{K_s} < -21.5$ mag (the parent sample) are shown: full spatial distribution (top panel), the Virgo cluster galaxies (bottom left-hand panel) and a zoom-in on the core of the Virgo cluster (bottom right-hand panel). The legend in the top panel describes the symbols in all plots showing galaxies in kinematic groups: a (no rotation), b (NRRs without special kinematic features), c (kinematically distinct cores, including CRCs), d (2σ peak galaxies) and e (RRs). Spiral galaxies are shown as logarithmic spirals. The large dotted circles in the bottom left-hand panel have a radius of $12°$ and encompass the same region as the dotted ellipse in the top panel. The Virgo cluster core is shown by the solid circle centred on M87 with $R = 0.5$ Mpc.

below the imposed limit of $0.5R_e$, making it a very small feature (see Appendix A).

In the Virgo cluster, the situation is alike: galaxies with the RR-type rotation and spirals are similarly distributed, although spirals tend to be farther from the centre of the cluster. In contrast, the galaxies with complex kinematics are mostly found in the very core of the cluster ($R < 0.5$ Mpc). Specifically, there are 11 galaxies from groups a, b, c and d and eight of them are within 0.5 Mpc in radius centred on M87. The three galaxies outside are NGC 4489 (north of the core), NGC 4472 (south of the core) and NGC 4733 (east of the core). NGC 4472 and 4489 are both classified as CRC galaxies,

but NGC 4472 (or M49) is in a more densely populated environment and it is the most massive galaxy of a small subgroup, while NGC 4489 is in a region with a fewer larger galaxies. NGC 4733, also in a less densely populated region, was mentioned above as a barred galaxy.

A version of Fig. 4 showing the fast/slow rotators instead of our five kinematic classes is presented in Cappellari et al. (2011b, hereinafter Paper VII). We refer to that paper for a detailed investigation of the connection between the environment and kinematics of early-type galaxies. In Paper VII, we find a clear excess of slow rotators in the densest core of the Virgo cluster. The distribution of

galaxies with complex kinematics we find here (groups a, b, c and d) confirms that the environmental effects on the internal dynamics are significant.

4 DETERMINATION OF KINEMATIC AND PHOTOMETRIC POSITION ANGLES AND ELLIPTICITIES

In this section, we present methods for determining global values of the kinematic and photometric PAs as well as the global ellipticity of galaxies. All values are tabulated in Table D1.

4.1 Kinematic position angle

The global kinematic PA (PA_{kin}) is the angle which describes the orientation of the mean stellar motion on a velocity map. It is usually defined as the angle between the north and the receding part of the velocity map (maximum values). If the figure rotation is absent, PA_{kin} is also perpendicular to the orientation of the apparent angular moment (Franx 1988). We measure it using the method outlined in appendix C of Krajnović et al. (2006).[3] Briefly, for any chosen PA_{kin} we construct a bi-(anti)symmetric velocity map mirrored around an axis with the position angle $PA_{kin} + 90°$. The best PA_{kin} is defined as the angle which minimizes the difference between the symmetrized and the observed velocity maps.

The error on PA_{kin} is defined as the smallest opening angle that encloses the PAs of all the models for which the symmetrized and observed data are consistent within a chosen confidence level. The acceptable confidence level was defined by $\Delta\chi^2 < 9 + 3\sqrt{2N}$, where $\Delta\chi^2 < 9$ is the standard 3σ level for one parameter, and we included an additional term $3\sqrt{2N}$ to account for the 3σ uncertainties in χ^2. The latter term becomes important when dealing with large data sets, as pointed out in a similar context by van den Bosch & van de Ven (2009).

We produce 361 different bisymmetrized maps with $0°.5$ steps in the PA ranging from $0°$ to $180°$. The actual uncertainty also depends on the bin sizes, FoV, asymmetric coverage of the galaxy and velocity errors (see Section 4.3). In addition, we compare and verify our results with the radial profiles of Γ_{kin}[4] derived using KINEMETRY (see Section 3). As was also shown in Krajnović et al. (2006), the average luminosity weighted $\overline{\Gamma_{kin}}$ obtained from KINEMETRY agrees well with the global PA_{kin} for a typical velocity map.

4.2 Photometric position angle and ellipticity

The photometric position angle (PA_{phot}) measures the orientation of the stellar distribution and it defines the position of the apparent photometric major-axis measured east of north. We derive PA_{phot} by calculating the moments of inertia of the surface brightness distribution from the SDSS and INT r-band images. At the same time, the method provides the global ellipticity ϵ. PA_{phot} and ϵ estimated in this way are dominated by large scales. This is favourable since we want to derive the orientation and the shape representative of the global stellar distribution, particularly to avoid the influence of the bars, which are usually restricted to small radii and are common in

our sample. For this reason, we also try to use the largest possible scales of the images.

We first determine the median level and the root mean square (rms) variation of the sky in each image. We then use an IDL routine that measures the moment of inertia[5] on pixels that are a few times the sky rms above zero (a median sky level was subtracted from the images). We masked the bright stars and companion galaxies if present. As levels we use 0.5, 1, 3 and 6 times the sky rms. The standard deviation of the measurements at these levels is used to estimate the uncertainties to PA_{phot} and ϵ. Final ϵ and PA_{phot} are taken from the measurement obtained using pixels that were three times the rms. In some cases, most of the galaxy surface brightness is dominated by the bar and in order to probe the underlying disc, one has to encompass the faint outer regions. In these cases, depending on the size of the bar, we use the measurements obtained at lower sky cuts, 0.5 or 1 time the sky rms. In this way, PA_{phot} was typically measured between 2.5–3 effective radii.

We also fitted ellipses to the isophotes of our galaxies and obtained radial profiles of the position angle Γ_{phot} and the flattening q_{phot} using the KINEMETRY code optimized for the surface photometry. We compared the results of the moment of inertia method with the averages of the rings between the sky level and a level at six times the sky rms. The standard deviations of the differences between the two estimates for PA_{phot} and ϵ were $2°$ and 0.03, respectively. A special care should be given to the estimate of ϵ, particularly when $\epsilon \sim 0$, as ellipticity values are bound (>0), which induces a positive bias at low ellipticities. We estimated this bias by constructing round models with de Vaucouleurs profiles, using brightness, noise patterns and sky backgrounds similar to the observed galaxies. Our tests suggest that the moments of inertia method affects the estimate of ϵ by a positive bias of about 0.02.

4.3 Uncertainties on PA estimates

The uncertainties for both PA_{kin} and PA_{phot} are, generally, small, as can be seen from Fig. 5. In the case of the photometry (upper panel), there is an expected trend of larger errors with decreasing ellipticity, since PA_{phot} is not a defined quantity for a circle. For $\epsilon > 0.4$, the mean measured uncertainty is just under $2°$, while for $\epsilon < 0.4$ it increases to just above $9°$. Most of the galaxies with larger uncertainties are either barred/ringed, interacting or dusty systems. Similarly, in the case of kinematics (lower panel), there is a clear trend of increasing errors with decreasing maximum rotational velocity observed within the SAURON FoV. The average uncertainty on PA_{kin} for systems with $k_1^{max} > 100\,km\,s^{-1}$ is just above $3°$, while for $k_1^{max} < 100\,km\,s^{-1}$ the mean error is $17°$. The existence of bars/rings or the evidence for the interaction does not influence the accuracy of PA_{kin} determinations. Dust has some influence, but it is the disappearance of the rotation that causes the large uncertainties in PA_{kin}.

Measurements by the moment of inertia method can be systematically biased by the dust obscuration, interaction features (shells, tidal streams, accreted components), morphological features (bars, rings) and bright stars or companion galaxies. Most of our galaxies are dust free and when present, dust is mostly centrally distributed. Bright stars can be avoided in most cases by masking, which usually also works well on companion galaxies, unless the pairs are very close. On the other hand, going out to large scales to avoid bars

---

[3] We use an IDL routine fit_kinematic_pa.pro publicly available at http://www.purl.org/cappellari/idl

[4] Note that we differentiate between the global and local kinematic orientations, PA_{kin} and Γ_{kin}, respectively, estimated with different methods. The same applies for the photometric values.

[5] The IDL routine is called find_galaxy.pro and is a part of the MGE package (Cappellari 2002) that can be found at http://www.purl.org/cappellari/idl
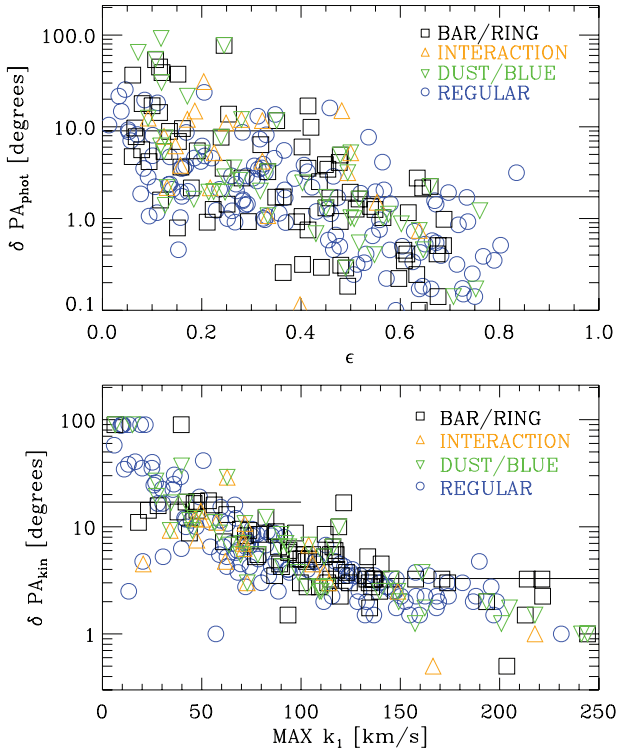
Figure 5. Top panel: the uncertainty on the photometric position angle, δPA$_{phot}$, as a function of the ellipticity. Bottom panel: the uncertainty on the kinematic position angle, δPA$_{kin}$, as a function of the maximum rotational velocity reached within the SAURON FoV. The horizontal lines on both panels show mean uncertainty values for the region they cover. In the top panel: $\sim 9°$ for $\epsilon < 0.4$ and $\sim 2°$ for $\epsilon > 0.4$. In the bottom panel: $\sim 17°$ for $k_1^{max} > 100\,km\,s^{-1}$ and $\sim 3°$ for $k_1^{max} > 100\,km\,s^{-1}$. The black squares show galaxies with bars and/or rings, orange upward-pointing triangles show galaxies with an evidence for interactions, green downward-pointing triangles show galaxies with an evidence for dust or blue nuclei and other, regularly looking early-type galaxies are shown with the blue circles.

Figure 6. Top panel: an estimate of the photometric radial variation of Γ^{VAR}_{phot} plotted as a function of the ellipticity. Bottom panel: an estimate of the kinematic radial variation of Γ^{VAR}_{kin} plotted as a function of the maximal rotational velocity within the SAURON FoV. The dashed horizontal lines in both panels are at 5°. The black squares are galaxies with bars and/or rings. The orange upward-pointing triangles show interacting systems. The green downward-pointing triangles show galaxies with an evidence for dust or blue nuclei. In the top panel, regularly looking early-type galaxies are shown with the blue circles. In the bottom panel, the red diamonds show galaxies from kinematic groups a, b, c and d with the regular morphology. Galaxies from group e with regular morphologies are shown with the blue circles.

increases the probability to detect shells and brighter tidal debris in other galaxies. It is possible to avoid both problems if there is no a priori set radius at which (PA$_{phot}$, ϵ) are measured, but an optimal one is chosen for each object instead. This, however, has to be taken into account during the analysis of the data and could be revised for different purposes.

In the case of PA$_{kin}$, the main sources of systematic errors lie in the contamination by foreground stars, dust lanes, large bin size or bad bins. The stars or bad bins can be masked leaving enough information to determine PA$_{kin}$, while the dust affects the overall velocity extraction. Dusty galaxies are uniformly distributed over the parameter ranges plotted in Fig. 5 and there is no evidence that the dust is affecting our measurements significantly. Large bins, however, mean a simple loss of the spatial resolution and a degradation in the PA$_{kin}$ precision. We estimate that in about 5 per cent of galaxies, PA$_{kin}$ might be affected to some degree by the lower spatial resolution. This effect is accounted for in the quoted uncertainties.

Finally, the estimated uncertainties do not fully reflect the actual radial variation in the PAs; the extent of isophotal or kinematic twists is only partially represented with our derived uncertainties, especially in the case of the photometry where the measurements are biased to the larger radii. In Fig. 6, we show a measure of the PA twists for both photometric and kinematic data from the KINEMETRY
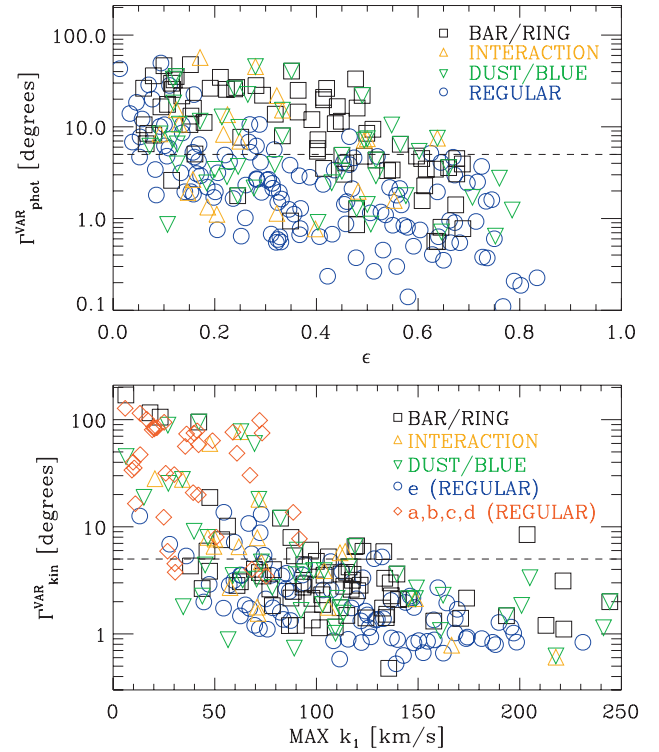
analysis of the images and the velocity maps. They were estimated as the standard deviation within $1R_e$ or the SAURON FoV, Γ^{VAR}_{phot} and Γ^{VAR}_{kin} for photometric and kinematic radial variations, respectively. In the case of photometry (upper panel), galaxies with larger Γ^{VAR}_{phot} are typically barred, but there are also interacting systems or galaxies with dust. Note that regular, undisturbed galaxies with larger Γ^{VAR}_{phot} mostly have small ellipticities, which is also a consequence of the degeneracy in the PA determination for more round objects.

In the case of kinematics (lower panel), radial variations are seen almost exclusively in galaxies with the NRR type of rotation, which also have lower maximal rotational velocities. These galaxies typically harbour KDC and CRC features (Γ^{VAR}_{kin} around 90°). Note that for NRR galaxies with large Γ^{VAR}_{kin} not all values should be taken at their face values. The KINEMETRY results are not robust in the regime when the rotation drops below the measurement level and the ellipse parameters are poorly constrained.

We conclude this section by taking as the typical uncertainty on PA$_{phot}$ and PA$_{kin}$ a value of 5°. This is a small overestimate for flat and fast-rotating systems, while somewhat less accurate for round and slow-rotating galaxies, and we note that the typical uncertainty on PA$_{kin}$ is somewhat larger than the typical error on PA$_{phot}$. We will use it as the representative uncertainty when the two measurements are combined in the next section.
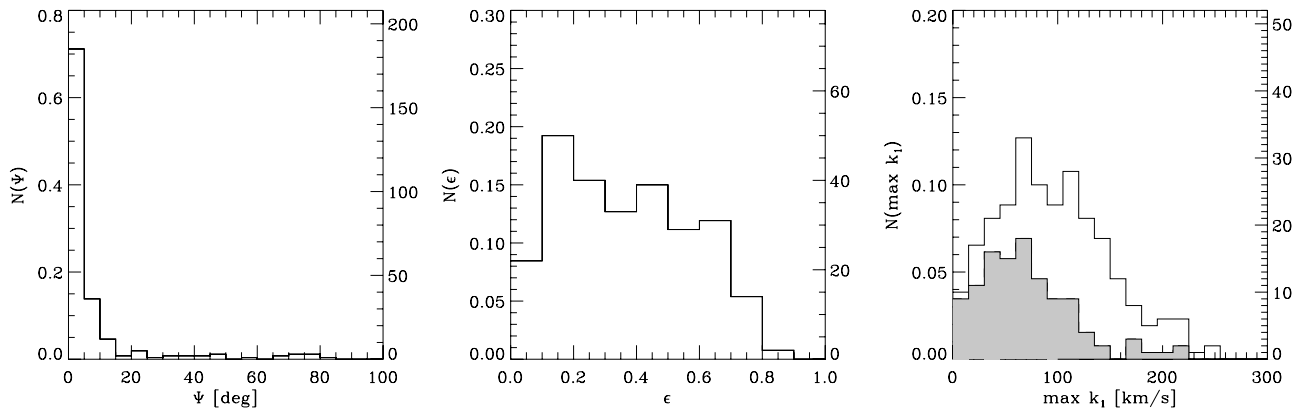
Figure 7. From the left-hand to right-hand panel: histograms of the kinematic misalignment angle, ellipticity and maximum rotational velocity. The left-hand y-axis is normalized to the total number of galaxies, while the right-hand y-axis gives the number of objects in each bin. In the rightmost histogram, the shaded region is for galaxies with $\epsilon \leq 0.3$.

5 KINEMATIC MISALIGNMENT

Based on the Franx et al. (1991) definition, we calculate the kinematic misalignment angle Ψ as the difference between the measured photometric and kinematic PAs:

$$\sin \Psi = |\sin(PA_{phot} - PA_{kin})|. \qquad (1)$$

In this way, Ψ is defined between two observationally related quantities and it approximates the true kinematic misalignment angle, which should be measured between the intrinsic minor-axis and the intrinsic angular momentum vector. In the above parametrization, Ψ lies between $0°$ and $90°$, and it is not sensitive to differences of $180°$ between PA_{phot} and PA_{kin}.

In Fig. 7, we show histograms of three quantities for galaxies in the ATLAS^{3D} sample. The kinematic misalignment angle Ψ is remarkably uniform: 71 per cent of galaxies are in the first bin with $\Psi \leq 5°$, with another 14 per cent with $5° < \Psi \leq 10°$, and in total 90 per cent of galaxies having $\Psi \leq 15°$. The remaining 10 per cent of galaxies are spread over $75°$ with a few objects per bin. Before exploring in more details below the remarkable *near alignment* of early-type galaxies, we note a relatively flat distribution of ellipticities and the broad distribution of the maximum rotational velocity centred at about $90 \, \mathrm{km \, s^{-1}}$.

The distribution of ellipticities of ATLAS^{3D} galaxies is different from the distributions of ellipticities of both 'ellipticals' and 'spirals' measured in the SDSS data (Padilla & Strauss 2008). Our galaxies span the ellipticity range from 0 to just above 0.8 and in that sense is similar to the apparent shape distribution of spirals. There is, however, an excess of round objects relative to the late types and an excess of flat objects relative to the early types from samples analysed by Padilla & Strauss (2008). An in-depth analysis of the distribution of ellipticities in the ATLAS^{3D} sample and its inversion regarding the intrinsic shape distribution will be a topic of another paper in this series.

The distribution of maximum rotational velocities can be described as a broad distribution around $90 \, \mathrm{km \, s^{-1}}$ and a tail of objects with high velocities. Our sample is different from the sample of Franx et al. (1991) where most of the galaxies have the rotational velocity less than $100 \, \mathrm{km \, s^{-1}}$, with a peak at $\sim 40 \, \mathrm{km \, s^{-1}}$. This is naturally explained by the fact that their sample had galaxies with $\epsilon < 0.3$, as it can be seen if we plot the histogram of k_1^{max} for only those galaxies (shaded region in the bottom panel).

In the top panel of Fig. 8, we show the kinematic misalignment angle as a function of the ellipticity for all galaxies in the sample

(in the second panel from the top, we show the same data, but without the error bars and Ψ in the range of $0°$–$40°$). The seven larger symbols plotted as upper limits are the galaxies which do not show rotation (kinematic group a). Their uncertainties on PA_{kin} are typically $\sim 90°$ and the values of their Ψ are unconstrained; hence, in this figure, we plot them as 'upper' limits.

While most of the galaxies are aligned, there is a dependence of Ψ on ϵ, in the sense that rounder objects are more likely to have larger Ψ. At the same time, however, the uncertainties increase, as shown in Section 4.3. In this section, we want to scrutinize the galaxies with an evidence for the kinematic misalignment and, based on the results of Fig. 5, we look in more details only at galaxies with $\Psi > 15°$.

In the two top panels of Fig. 8, we also highlight the positions of galaxies with different morphological features. Most of the galaxies with resonance phenomena have small Ψ. The five most misaligned galaxies are: NGC 502, 509, 2679, 4268 and 4733. NGC 4733 was mentioned before (see Section 3.2.4). The other four galaxies are characterized by relatively poor kinematic data quality. NGC 502 and 2679 have shapes similar to NGC 4733, but NGC 2679 also has a prominent ring. NGC 509 and 4268 are interesting since they are the only galaxies flatter than 0.3 with a significant misalignment. NGC 4268 has evidence for a ring, while NGC 509 has a peanut-shaped bulge. Except in the central $\sim 10 \times 5$ arcsec^2, their velocity maps are dominated by large bins with significant changes in the velocity between them, which can bias the determination of PA_{kin} and might explain the unusually large Ψ of these flattened objects.

Dust or blue nuclear features are present in galaxies that are generally aligned; there are four galaxies in this class with a significant misalignment: NGC 3073 (see Section 3.2.4), 1222, 3499, 5631 and 5485. NGC 1222 is an interacting galaxy with complex dust features and most likely not a settled object yet. NGC 3499 has a twisted dust lane which is almost perpendicular to the observed rotation. NGC 5631 has a dust disc associated with the rotation of the KDC, while NGC 5485 is one of two long-axis rotators[6] in our sample (Wagner, Bender & Moellenhoff 1988). It also has a dust disc of ~ 27 arcsec in size (just smaller than the effective radius of 28 arcsec and fully covering the SAURON FoV), which is oriented

---

[6] Sometimes the long-axis rotation is also called the prolate rotation. In general, the prolate rotation is characterized by the difference between the global photometric and kinematic PAs of $\sim 90°$.
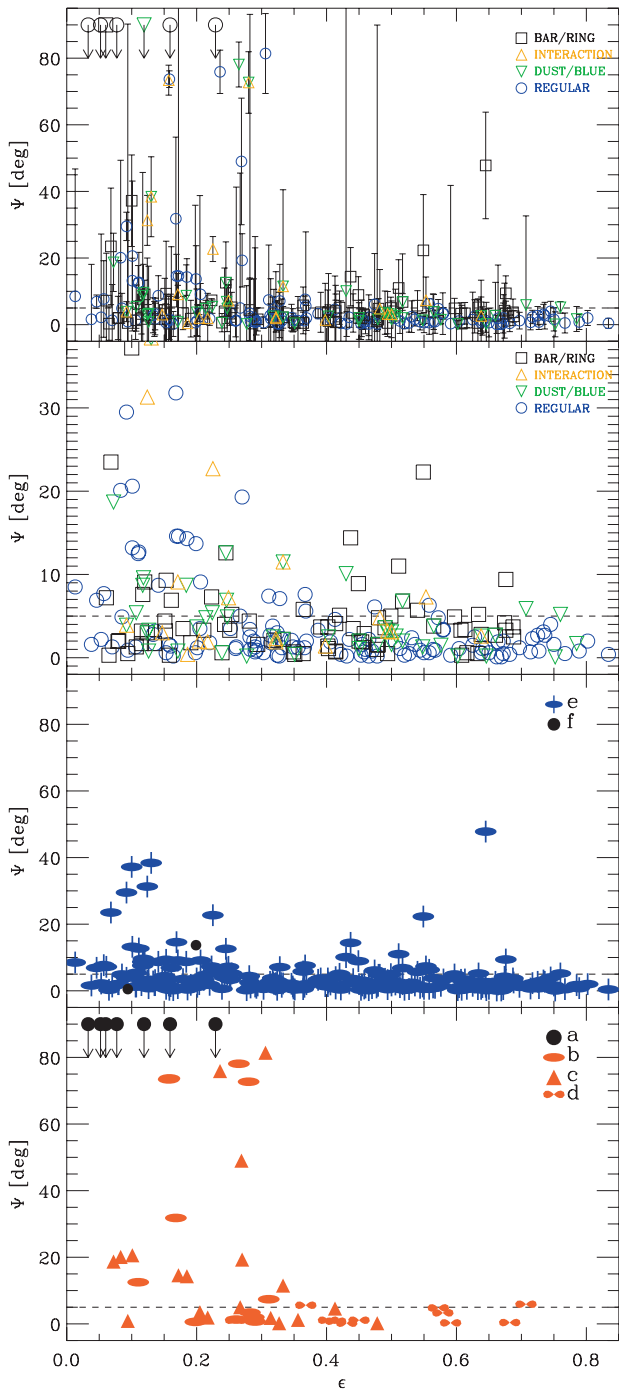
Figure 8. Distribution of the kinematic misalignment angle Ψ as a function of the ellipticity ϵ. Top panel: all galaxies. Different morphological features are shown with different symbols: black squares show galaxies with bars and/or rings, orange upward-pointing triangles show galaxies with interaction features, green downward-pointing triangles show galaxies with dust or blue nuclei, blue circles show galaxies without specific features. Large symbols without error bars show galaxies without detectable rotation (kinematic group a). The error bars are the uncertainties of PA$_{\rm kin}$. Middle top panel: the same plot as above, but where Ψ spans only 40° and without the error bars for clarity. Middle bottom panel: the kinematic misalignment of galaxies in kinematic groups e (RRs) and f (unclassified kinematics). Bottom panel: the kinematic misalignment of galaxies with complex kinematics belonging to groups: a (no rotation), b (NRRs without special kinematic features), c (kinematically distinct cores, including CRCs) and d (2σ peak galaxies). In the bottom two plots, the error bars are not plotted for clarity.

along the minor-axis, making it a polar dust disc aligned with the stellar rotation.

Similarly, there are five strongly misaligned galaxies with interaction features: NGC 474 (Turnbull, Bridges & Carter 1999), 680, 1222, 3499 and 5557. Of these, all but NGC 1222 and 3499 are characterized by shells, while these systems are also dusty. All other galaxies with Ψ > 15° (NGC 4261, 4278, 4365 4406, 4458, 5198, 5481, 5813 and 5831) have the normal morphology for early types, but they, except NGC 4278 (see below), belong to kinematic groups b and c.

In conclusion, misaligned systems often have bars, rings, dust and interaction features, and there are indications that these morphological structures influence the measurements of PA$_{\rm phot}$. They certainly highlight a complex and, in some cases, also unsettled internal structure. Misaligned galaxies with the normal morphology have complex kinematics to which we turn our attention now.

The middle bottom panel of Fig. 8 shows the kinematic misalignment angle for galaxies belonging to kinematic group e. These are all galaxies with simple regular rotations that can be well described by the cosine law. These galaxies are evenly spread in ϵ but are mostly found with small Ψ and constitute the majority of galaxies in the first bin of the kinematic misalignment histogram (left-hand panel in Fig. 7). There are, however, a few that are strongly misaligned (in the order of decreasing Ψ): NGC 509, 3499, 502, 474, 4278, 2679, 680 and 4268. Of these only NGC 4278 was not previously mentioned. Although this galaxy is classified as a RR, its kinematics show some peculiar signatures (Schechter & Gunn 1979; Davies & Birkinshaw 1988; van der Marel & Franx 1993; Emsellem et al. 2004): the mean velocity is decreasing towards the edge of the SAURON FoV and we do not cover the full effective radius. In that respect, the rotation that we are seeing could also belong to a large KDC covering the FoV and it could change significantly outside the covered area (see discussion in Appendix A). This galaxy also shows a drop in the central velocity dispersion. All these suggest that it is a special case and could be classified as a KDC.

The lower panel of Fig. 8 shows galaxies with complex kinematics and there is a significant number of strongly misaligned galaxies. We show again the galaxies from kinematic group a (no rotation) as upper limits since their actual positions in the Ψ–ϵ diagram is unconstrained. A Kolmogorov–Smirnov (K–S) test (Press et al. 1992) rejects the hypothesis that the galaxies from group e on the panel above have the same distribution of Ψ as the galaxies from groups b, c and d in this panel (the probability that the distributions are the same is 0.001).

Galaxies of kinematic group b (NRRs with no kinematic features) are found both among the aligned (six) and misaligned (six) objects. Some of the most misaligned objects fall in this group, such as the long-axis rotators NGC 4261 and 5485. A similar spread in Ψ is found in galaxies of kinematic group c, which comprises KDC and CRC systems. The only somewhat misaligned CRC system is NGC 4472 (Ψ = 14°), while the alignment of the KDC is rare. It happens in some of those KDC galaxies which do not have any rotation outside the core, when the rotation of the KDC is aligned with the global shape of the galaxy.

The final group of objects in this panel is group d (2σ peak galaxies). They are all aligned systems and except in two cases they are found only at ϵ > 0.4, where there are typically no misaligned galaxies. Their velocity maps are often characterized by counter-rotating components and in terms of the kinematic misalignment they are similar to CRC galaxies (but see the discussion in Appendix A).

We looked for the dependence of the kinematic misalignment angle on both the environment and the galaxy mass, but found

no strong correlations. Defining the measure of the environment as the density inside a sphere containing the 10 nearest galaxies (Paper VII), we found no statistical difference in Ψ for galaxies between the inside and outside of the Virgo cluster (a K–S test probability is 0.192). On the other hand, galaxies with $\Psi > 15°$ are often found in intermediate environments with the number densities ranging from 0.01–0.1 Mpc^{-3}. The kinematic misalignment does not depend on the mass strongly; however, splitting the sample at $10^{11.2}$ M$_\odot$ yields a K–S test probability of 0.007, suggesting that only the most massive galaxies in our sample are more misaligned than other systems. Note that the group of most massive galaxies contains the majority of galaxies for which Ψ is unconstrained (i.e. non-rotators), which were not used in the statistical tests.

6 DISCUSSION

The two most striking findings of this work are that (i) among nearby early-type galaxies 82 per cent show ordered RRs and that (ii) 72 per cent are systems with an alignment between the photometry and kinematics of less than 5°, while 90 per cent are consistent with this value when the uncertainties are taken into account. There are only 10 per cent of galaxies with a large misalignment ($\Psi > 15°$). This finding contradicts the canonical picture of early-type galaxies and in this section we discuss our results in more detail.

6.1 Consequence of the kinematic alignment of early-type galaxies

The axial symmetry is the rule rather than an exception among early-type galaxies, at least within one effective radius. This is in contrast with the conventional view of early-type galaxies, in particular ellipticals. Our understanding of their structure changed from considering ellipticals simple in shape, containing little gas or dust and dynamically uncomplicated one-component systems (e.g. Gott 1977) to being dynamically complex, kinematically diverse and morphologically heterogeneous (e.g. Binney 1982; Kormendy & Djorgovski 1989; de Zeeuw & Franx 1991; Jaffe et al. 1994; Faber et al. 1997; Kronawitter et al. 2000; Emsellem et al. 2004; Kormendy et al. 2009). The first systematic observations with IFSs and the analysis of two-dimensional kinematic maps confirmed the complexity of early-type galaxies, but also showed that the traditional separation into ellipticals and lenticulars is not able to find out the kinematic and dynamic difference between these objects (Cappellari et al. 2007; Emsellem et al. 2007). Specifically, half of the ellipticals in the SAURON sample were kinematically similar to lenticulars and a fraction of the other half showed signatures of triaxiality. The ATLAS^{3D} sample, comprising all early-type galaxies brighter than $M_{K_s} < 21.5$ and within $D < 42$ Mpc, is the first sample which can address this point statistically with IFS data.

The majority of early-type galaxies are still relatively simple systems (group e with 80 per cent of galaxies). Their velocity maps are mostly featureless and similar to those of thin discs, although they might have multiple kinematic and morphological components, such as inner discs, bars or rings. Their apparent angular momenta are typically aligned with the projected minor-axis of the stellar distribution, suggesting close to axisymmetric shapes. Galaxies from group e, which show misalignments, are typically barred, have dusty features (both of which can influence the measurement of the PAs) or exhibit evidence for recent interactions (i.e. they are either not fully settled systems and/or the measurements of the PAs might be biased).

A minor fraction of early-type galaxies show complex kinematic maps and a variety of kinemetric features (groups a, b, c and d with ~20 per cent of galaxies). They have multiple components with appreciably different kinematic properties (e.g KDC), some show no detectable rotation, while in others, the rotation is present, but it is quantitatively different (measured by KINEMETRY) from the regular pattern of the majority of objects. Approximately, half of the kinematically complex galaxies are significantly misaligned. As in galaxies from group e, there are cases of dusty or interacting galaxies with large Ψ, but the majority of misaligned galaxies with complex kinematics seem to be morphologically undisturbed objects and the kinematic misalignment is an evidence for their triaxial figure shapes.

The median kinematic misalignment angle for our sample is ~3° which is quite different from the predictions of hierarchical structure formation models (e.g. van den Bosch et al. 2002; Bailin & Steinmetz 2004, 2005; Croft et al. 2009; Bett et al. 2010), although the comparison between the cosmological simulation results and the observations cannot be made directly, given the differences in methods, probed regions and the content of simulated and observed galaxies. The comparison with the Ψ values from the remnants of mergers of equal-mass discs shows that smaller misalignments are found if the mergers are dissipational (Cox et al. 2006; Jesseit et al. 2009), where the increase in the gas content helps to align the angular momenta with the orientations of the minor-axes of the merger remnants (Hoffman et al. 2010), but it also depends on the type of orbits of the merger and the actual Hubble type of the progenitors (Bois et al. 2011, hereinafter Paper VI). Furthermore, the remnants of unequal mass mergers are typically aligned (Cox et al. 2006; Jesseit et al. 2009; Paper VI) and they are likely to be significant among the formation processes for the formation of the present-day population of early-type galaxies.

Within 42 Mpc, there are about 9 per cent of misaligned early-type galaxies or less than 3 per cent of the total galaxy population. This suggests that the processes that result in large Ψ measured between ~1 (kinematics) and ~3 (photometry) effective radii cannot be very important for the formation of the majority of early-type galaxies, although they are likely important at the high-mass end of the galaxy distribution.

6.2 Discs in early-type galaxies

The majority of early-type galaxies show RR type rotation, characterized by velocity maps similar to those of inclined discs [$V = V_{rot}\cos(\theta)$], having either featureless RR/NF velocity maps (66 per cent of the sample) or two-component RR/2M velocity maps (14 per cent of the sample). The vast majority of these galaxies are also kinematically aligned. Furthermore, bars and rings, which occur in discs, are found almost exclusively in galaxies with this type of rotation.

As we show in Paper III, the division into the RR and NRR types of rotation can be used to help separate the early-type galaxies into fast and slow rotators, respectively. Cappellari et al. (2007) and Paper III show that fast rotators, or galaxies from kinematic group e, are consistent with being a single family of oblate objects viewed at different inclination angles. These results indicate that RR galaxies are, at least to a first approximation, made of flattened, rapidly rotating components which must be related in their origin to discs.

Multiwavelength observations show that the gas is often present in early-type galaxies and it is frequently settled in discs, both large H I and small CO or ionized gas discs (e.g. Morganti et al. 2006;

Sarzi et al. 2006; Serra et al. 2008; Young et al. 2008; Oosterloo et al. 2010). Other papers in this series will discuss these aspects in more detail, but we stress that the gas is important for the evolution of many (if not most) early-type galaxies. In addition, the stellar population content of RR galaxies often shows distinct and flattened regions of increased metallicity, suggesting a link with regions of ordered rotation (Kuntschner et al. 2006, 2010).

The disc-like origin of kinematics is also visible in the higher order moments of the LOSVD, usually parametrized by Gauss–Hermite moments, which describe the deviations from a Gaussian shape of the absorption-line profiles (Gerhard 1993; van der Marel & Franx 1993). In Fig. 9, we show h_3 Gauss–Hermite moments separating the galaxies according to their kinematics and morphology, plotting values for each spatial bin (spectra) of those galaxies with the effective velocity dispersion $\sigma_e > 120 \, \text{km s}^{-1}$ (151 galaxies). This selection is made to avoid possible biases for galaxies with σ_e close or lower than the SAURON spectral resolution (see Paper I for details on the extraction of kinematics). The anticorrelation between h_3 and V/σ, which is indicative of disc kinematics (e.g. Bender et al. 1994), is most strongly visible in galaxies belonging to the RR kinematic class. Galaxies with the NRR type of rotation from kinematic groups a, b and c do not show such anticorrelation, although there is a hint that among the group c galaxies (KDC and CRC) there are cases (or regions) with a certain $V/\sigma - h_3$ anticorrelation. It is very interesting to see that galaxies with 2σ peaks actually show the anticorrelation. In general, the trends are governed by the spread in V/σ values: galaxies with the RR type of rotation have large values of V/σ, which is not the case for galaxies with the NRR type of rotation. This property is illustrated in Paper III. Note that in this respect 2σ objects are different from other galaxies with complex kinematics (groups a, b and c): the range of V/σ they cover is smaller than in RR galaxies, but it is bigger than for NRR galaxies.

Bars are created from disc instabilities and it is expected that the kinematics of galaxies with bars and/or rings also show the $h_3 - V/\sigma$ anticorrelation. There are, however, significant differences between RR galaxies with and without resonances: the extent of V/σ is somewhat smaller in galaxies with bars/rings, but there is also evidence for a correlation between h_3 and V/σ, which can be seen in the excess of points at negative/positive V/σ and negative/positive h_3 values. The existence of these correlated points is related to the correlation between h_3 and V, typical for barred galaxies and peanut bulges (Chung & Bureau 2004; Bureau & Athanassoula 2005)

Fig. 10 shows h_4 Gauss–Hermite moments of the LOSVD for galaxies separated in the same way as in the previous figure. Again there are some differences between galaxies with the RR and NRR type of rotation. In RR galaxies for large V/σ, h_4 values are typically smaller and positive, but the distribution is not symmetric. This is especially notable for galaxies with bars/rings, while the averages of the h_4 distributions are, in general, slightly positive.

The $h_3 - V/\sigma$ anticorrelation is reproduced in the cosmological simulation (Naab et al. 2007), as well as in simulations of major mergers, where the amount of the gas and relative mass ratios (e.g. 1:1, 2:1, 3:1) determine shapes of the $h_3 - V/\sigma$ and $h_4 - V/\sigma$ distributions that, generally, agree well with the observations (González-García, Balcells & Olshevsky 2006; Naab et al. 2006). Hoffman et al. (2009) present the latest detailed predictions for the $h_3 - V/\sigma$ and $h_4 - V/\sigma$ distributions for one-to-one disc mergers of varying gas fractions (from 0 to 40 per cent). The major merger simulations reproduce some aspects of Figs 9 and 10. The $V/\sigma - h_3$ anticorrelation in gas-rich mergers (starting from 15 per cent of gas) resembles the distribution of points for galaxies of group e without bars and/or rings. Similarly, to some extent the quantitative shape of $V/\sigma - h_4$ diagrams for large gas fractions also resembles the observations of galaxies of group e without resonances. In both cases, however, the V/σ range is smaller in the simulation than in the observations, with
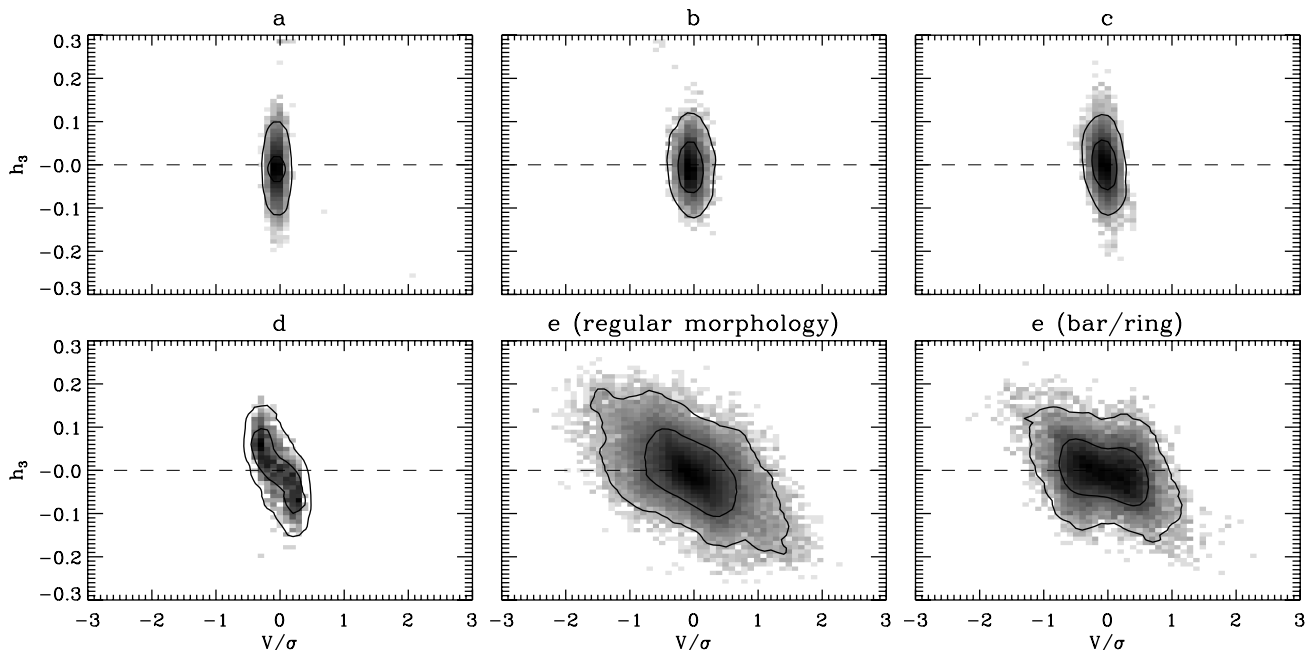
Figure 9. Local $h_3 - V/\sigma$ relation for every spectrum in galaxies with $\sigma_e > 120 \, \text{km s}^{-1}$ and an error on $h_3 < 0.05$. Shown are values in bins of 0.1 in V/σ and 0.01 in h_3. The colour scale is proportional to the logarithm of the intensity where the entire map sums to one. Contours enclosing 68 and 95 per cent of the distributions have been smoothed using a boxcar filter and a window of 2 pixels in both dimensions. Different panels show values for galaxies separated according to their kinematics or morphology. From the top to bottom (right-hand to left-hand side): LV galaxies (group a), NRR galaxies (group b), KDC galaxies (group c), galaxies with 2σ peaks (group d), RR galaxies (kinematic group e) without bars and/or rings and RR galaxies with bars and/or rings.
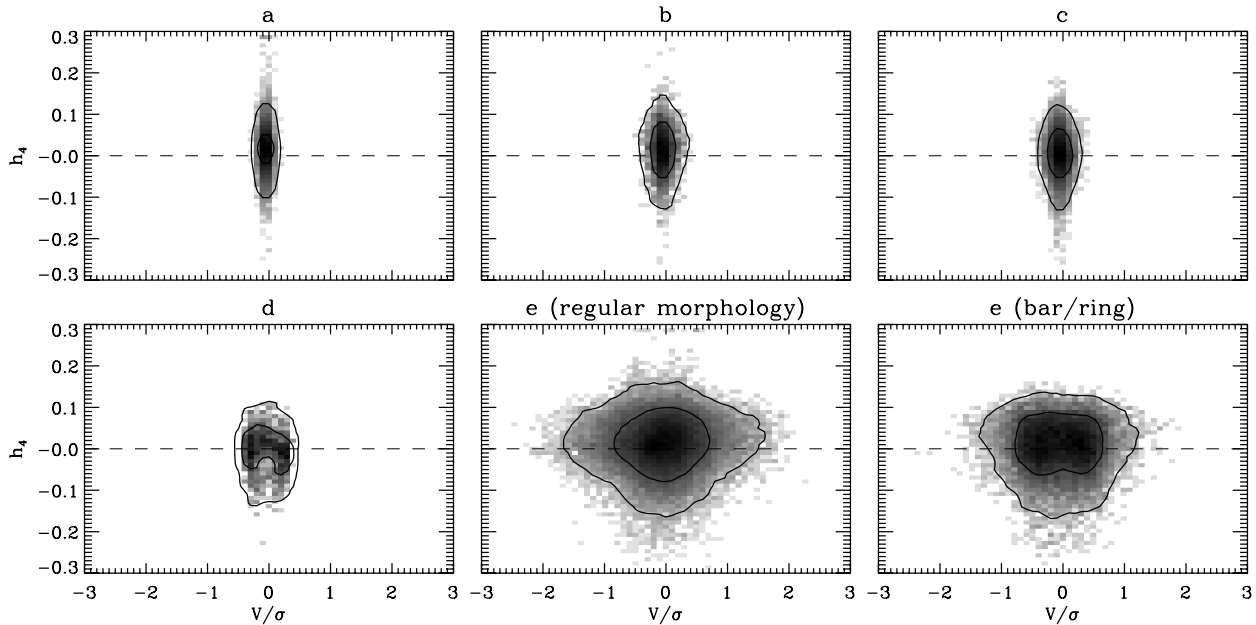
Figure 10. Local h_4–V/σ relation for every spectrum in galaxies with $\sigma_e > 120\,\mathrm{km\,s^{-1}}$ and an error on $h_4 < 0.05$. Different panels show values for galaxies separated according to their kinematics of the morphology as in Fig. 9. The colour scheme and the contours are the same as in Fig. 9.

the simulations predicting overall a narrower distribution for h_3 and tails of positive h_4 values, which are not seen in the observations. It seems that the merger remnants do not rotate fast enough to reproduce the population of the RR-type galaxies, but rotate too fast to reproduce galaxies with the NRR-type rotation, at least within one effective radius. In contrast, the products of the consecutive dry mergers of the remnants (of the initial one-to-one mergers with 20 and 40 per cent gas) better reproduce the observations, especially the fact that V/σ is small.

One should also keep in mind that the similarities between gas-rich merger remnants and the RR type of galaxies probably come from the fact that these types of mergers produce orbital structures (e.g. short-axis tubes) qualitatively similar to those allowed in nearly axisymmetric potentials of galaxies with the RR-type rotations (Jesseit, Naab & Burkert 2005; Hoffman et al. 2010), but it is not clear that they create the full spectrum of observed objects among the population of early-type galaxies, suggesting that other processes should also be addressed (e.g. Naab, Khochfar & Burkert 2006).

In summary, the kinemetric analysis of the velocity maps shows that the vast majority of early-type galaxies have the disc-like rotation. The distribution of kinematic misalignments suggests that a great majority of early-type galaxies are nearly axisymmetric or, if they are barred, are disc systems. Their kinematic properties are only partially reproduced by equal-mass mergers. These results suggest that the disc origins of early-type galaxies remain imprinted on the entire object. Among the multiple processes that can create early-type galaxies, we need to identify a division between those that create, on the one hand, triaxial and those that create, on the other hand, close to axisymmetric, disc-dominated remnants.

6.3 Caveats

The measured kinematic misalignment angle suggests that most early-type galaxies are nearly axisymmetric systems. This conclusion is based on the global (average) values for $\mathrm{PA_{kin}}$ and $\mathrm{PA_{phot}}$ not taking into account the local variations, and where scales for measuring the global values are limited by our instruments: SAURON FoV of about $1R_e$ and the SDSS imaging reaching about $3R_e$.

If one looks at objects individually, however, a number of galaxies show local departures from the axisymmetry, such as photometric and kinematic twists (e.g. Γ_{phot}^{VAR} and Γ_{kin}^{VAR}, respectively, in Fig. 6). In addition, at least 30 per cent of galaxies are barred (or have bar-induced phenomena) in our sample. These objects are related to discs, but they are not axisymmetric, where the departure from the axisymmetry depends on the strength of the perturbation. Finally, the strong kinematic misalignment in about 9 per cent of galaxies argues for the triaxial shape of their figures. In all of these cases, the internal orbital distribution is likely more complex than the one described by an exactly axially symmetric potential.

Our kinematic measurements are confined to the central parts. It is possible that observing kinematics even farther out one would start measuring larger misalignments as suggested by studies of planetary nebulae around early-type galaxies (Coccato et al. 2009), although these and similar studies also find galaxies that stay (approximately) aligned (Coccato et al. 2009; Proctor et al. 2009). It is, however, significant that we measure the kinematic and photometric PAs at different radii. To understand the full meaning of this result, it is necessary to gather kinematic observations covering a few effective radii of a larger sample of galaxies.

7 CONCLUSIONS

We performed an analysis of the ground-based *r*-band images and the kinematic maps of 260 nearby early-type galaxies from the volume-limited ATLAS[3D] sample. We used the images to determine the frequency of bars, interaction features and dust structures as well as to measure the global photometric PA (PA of the major-axis) and the apparent ellipticity of the galaxies. 30 per cent of nearby early-type galaxies have bars and/or resonant rings. About 8 per cent of galaxies show interaction features and non-fully-settled figures at large radii at the surface brightness limit of the SDSS images. Barred galaxies do not show interaction features at that level of the surface brightness. We also determined local variations of these parameters using the isophote fitting incorporated in the KINEMETRY

software. Typically, the global PA and ellipticity were measured by encompassing the stellar distribution within 2.5–3 effective radii.

The kinematic maps are the result of SAURON observations and they consist of maps of the mean velocity, the velocity dispersion, and the h_3 and h_4 Gauss–Hermite moments. We used velocity maps to measure the global kinematic PA (orientation of the velocity map). This angle was estimated using full maps, which typically cover one effective radius, except for the largest galaxies where they generally cover at least a half of the effective radius.

We analysed the velocity maps applying KINEMETRY and used the information on the radial variation of the kinematic PA, flattening of the maps, radial velocity profiles and higher order harmonic terms to describe the structures on the maps and classify the galaxies according to their kinematic appearance. In doing so, we also looked for specific features in the velocity dispersion maps. This resulted in a separation of galaxies according to their rotation types: RRs and NRRs. The main difference between these galaxies is that the former have velocity maps well described by the cosine law [$V = V_r \cos(\theta)$], typical for velocity maps of inclined discs. The classification was done within $1R_e$ or within the SAURON FoV if smaller. The ATLAS^{3D} sample separates into 82 per cent (214) RR galaxies, 17 per cent (44) NRR galaxies and two galaxies not classified due to low-quality data. This separation is used in Paper III as a basis for a separation between fast and slow rotators. The kinematic difference between RR and NRR galaxies is also seen in the dependence of the higher order Gauss–Hermite moments (h_3 and h_4) on V/σ.

Using KINEMETRY we characterized various kinematic features visible in the mean velocity maps and the velocity dispersion maps, such as no-feature (NF), double maxima (2M), kinematic twists (KT), kinematically distinct core (KDC), counter-rotating core (CRC), low-level velocity (LV) and double σ (2σ). In principle, all features could occur in galaxies with both the RR and the NRR types of rotation, but we find that RR galaxies are predominantly described as either NF (171) or 2M (36), while NRR galaxies are relatively equally distributed among NF (12), LV (seven), KDC (11), CRC (seven) and 2σ (seven). Note that there are five exceptions to this rule: one RR/CRC and four RR/2σ galaxies.

In order to systematize the various kinematic features, we classify galaxies in five kinematic groups that encapsulate the most-significant features: a (NRR/LV galaxies), b (NRR/NF galaxies), c (all KDC and CRC galaxies), d (all 2σ galaxies) and e (all RR galaxies, unless they have KDC, CRC or 2σ features). The most numerous is group e (209 galaxies) and the least numerous is group a (seven galaxies). We show that the galaxies in groups a, b, c and d are typically found in dense regions. This result is in agreement with the morphology–density relation of Paper VII.

Based on the global values for photometric and kinematic PAs, we derive the distribution of the apparent kinematic misalignment angle (Ψ), which is directly related to the angle between the apparent angular momentum and the projection of the short axis, and hence related to the angle between the intrinsic angular momentum and intrinsic short axis in a triaxial system. A general expectation is that a triaxial object will have a non-zero apparent kinematic misalignment angle.

Exploiting our IFS data, we find that a large majority of the galaxies are nearly aligned (71 per cent of galaxies have $\Psi \leq 5°$, while 90 per cent are consistent with being aligned, taking uncertainties into account). Most of the misaligned galaxies have the NRR type of rotation or have signatures of interactions at larger radii. A few are also barred.

The small kinematic misalignment found in a great majority of early-type galaxies implies that they are axisymmetric, although individual objects show evidence for triaxial shapes, or bars. These systems have velocity maps more similar to the spiral galaxy discs than to the remnants of equal-mass mergers. The latter appear to contribute to the formation of only a minor fraction of massive galaxies in the nearby Universe. Although our results are valid for the central baryon-dominated regions of nearby galaxies only, we conclude that the formation processes most often result in disc-like objects that maintain the (nearly) axisymmetric shape of the progenitors. Candidate processes for forming the large fraction of early-type galaxies therefore include minor mergers, gas accretion events, secular evolution and environmental influences. Much less frequently, the formation process produces an object with a triaxial figure. Most likely, this involves major mergers with or without the gaseous dissipation. The division of galaxies into the RR and NRR types and the kinematic groups can be used to infer the formation process experienced by a particular object.

REFERENCES

Abazajian K. N. et al., 2009, ApJS, 182, 543
Bacon R. et al., 2001, MNRAS, 326, 23
Bailin J., Steinmetz M., 2004, ApJ, 616, 27
Bailin J., Steinmetz M., 2005, ApJ, 627, 647
Begeman K. G., 1987, PhD thesis, Groningen University
Bender R., 1988a, A&A, 202, L5
Bender R., 1988b, A&A, 193, L7
Bender R., Moellenhoff C., 1987, A&A, 177, 71
Bender R., Nieto J., 1990, A&A, 239, 97
Bender R., Saglia R. P., Gerhard O. E., 1994, MNRAS, 269, 785
Bertola F., Capaccioli M., 1975, ApJ, 200, 439
Bett P., Eke V., Frenk C. S., Jenkins A., Okamoto T., 2010, MNRAS, 404, 1137
Binney J., 1982, ARA&A, 20, 399
Binney J., 1985, MNRAS, 212, 767
Bois M. et al., 2011, MNRAS, submitted (Paper VI)
Bureau M., Athanassoula E., 2005, ApJ, 626, 159
Cappellari M., 2002, MNRAS, 333, 400
Cappellari M., Copin Y., 2003, MNRAS, 342, 345
Cappellari M. et al., 2007, MNRAS, 379, 418
Cappellari M. et al., 2011a, MNRAS, 413, 813 (Paper I)
Cappellari M. et al., 2011b, MNRAS, in press (doi:10.1111/j.1365-2966.2011.18600.x) (Paper VII)
Carter D., 1978, MNRAS, 182, 797
Chung A., Bureau M., 2004, AJ, 127, 3192
Coccato L. et al., 2009, MNRAS, 394, 1249
Contopoulos G., 1956, Z. Astrophysik, 39, 126
Cox T. J., Dutta S. N., Di Matteo T., Hernquist L., Hopkins P. F., Robertson B., Springel V., 2006, ApJ, 650, 791
Crocker A. F., Jeong H., Komugi S., Combes F., Bureau M., Young L. M., Yi S., 2009, MNRAS, 393, 1255
Croft R. A. C., Di Matteo T., Springel V., Hernquist L., 2009, MNRAS, 400, 43
Davies R. L., Birkinshaw M., 1986, ApJ, 303, L45
Davies R. L., Birkinshaw M., 1988, ApJS, 68, 409
Davies R. L., Illingworth G., 1983, ApJ, 266, 516
Davies R. L., Efstathiou G., Fall S. M., Illingworth G., Schechter P. L., 1983, ApJ, 266, 41
de Vaucouleurs G., de Vaucouleurs A., Corwin H. G., Jr, Buta R. J., Paturel G., Fouque P., 1991, Third Reference Catalogue of Bright Galaxies. Springer-Verlag, Berlin
de Zeeuw P. T., 1985, MNRAS, 216, 273
de Zeeuw T., Franx M., 1991, ARA&A, 29, 239
de Zeeuw P. T. et al., 2002, MNRAS, 329, 513
Donas J. et al., 2007, ApJS, 173, 597
Dressler A., Sandage A., 1983, ApJ, 265, 664
Efstathiou G., Ellis R. S., Carter D., 1980, MNRAS, 193, 931
Emsellem E. et al., 2004, MNRAS, 352, 721
Emsellem E. et al., 2007, MNRAS, 379, 401
Emsellem E. et al., 2011, MNRAS, in press (arXiv:1102.4444, doi:10.1111/j.1365-2966.2011.18496.x) (Paper III)
Faber S. M. et al., 1997, AJ, 114, 1771
Franx M., 1988, PhD thesis, Univ. Leiden
Franx M., Illingworth G., Heckman T., 1989, ApJ, 344, 613
Franx M., Illingworth G., de Zeeuw P. T., 1991, ApJ, 383, 112
Franx M., van Gorkom J. H., de Zeeuw P. T., 1994, ApJ, 436, 642
Gerhard O. E., 1993, MNRAS, 265, 213
González-García A. C., Balcells M., Olshevsky V. S., 2006, MNRAS, 372, L78
Gott III J. R., 1977, ARA&A, 15, 235
Hoffman L., Cox T. J., Dutta S., Hernquist L., 2009, ApJ, 705, 920
Hoffman L., Cox T. J., Dutta S., Hernquist L., 2010, ApJ, 723, 818
Hubble E. P., 1936, Realm of the Nebulae. Yale University Press, New Haven
Illingworth G., 1977, ApJ, 218, L43
Jaffe W., Ford H. C., O'Connell R. W., van den Bosch F. C., Ferrarese L., 1994, AJ, 108, 1567

Jaffe W., Ford H., Ferrarese L., van den Bosch F., O'Connell R. W., 1996, ApJ, 460, 214
Jarrett T. H., Chester T., Cutri R., Schneider S., Skrutskie M., Huchra J. P., 2000, AJ, 119, 2498
Jedrzejewski R. I., 1987, MNRAS, 226, 747
Jedrzejewski R., Schechter P. L., 1989, AJ, 98, 147
Jesseit R., Naab T., Burkert A., 2005, MNRAS, 360, 1185
Jesseit R., Naab T., Peletier R. F., Burkert A., 2007, MNRAS, 376, 997
Jesseit R., Cappellari M., Naab T., Emsellem E., Burkert A., 2009, MNRAS, 397, 1202
Kondratev B. P., Ozernoi L. M., 1979, Soviet Astron. Lett., 5, 37
Kormendy J., Bender R., 1996, ApJ, 464, L119
Kormendy J., Djorgovski S., 1989, ARA&A, 27, 235
Kormendy J., Fisher D. B., Cornell M. E., Bender R., 2009, ApJS, 182, 216
Krajnović D., Cappellari M., de Zeeuw P. T., Copin Y., 2006, MNRAS, 366, 787
Krajnović D. et al., 2008, MNRAS, 390, 93
Kronawitter A., Saglia R. P., Gerhard O., Bender R., 2000, A&AS, 144, 53
Kuntschner H. et al., 2006, MNRAS, 369, 497
Kuntschner H. et al., 2010, MNRAS, 408, 97
Landsman W. B., 1993, in Hanisch R. J., Brissenden R. J. V., Barnes J., eds, ASP Conf. Ser. Vol. 52, Astronomical Data Analysis Software and Systems II. Astron. Soc. Pac., San Francisco, p. 246
Lauer T. R., 1985, ApJS, 57, 473
Laurikainen E., Salo H., Buta R., Knapen J. H., 2009, ApJ, 692, L34
Lupton R., Blanton M. R., Fekete G., Hogg D. W., O'Mullane W., Szalay A., Wherry N., 2004, PASP, 116, 133
McDermid R. M. et al., 2006, MNRAS, 373, 906
Markwardt C. B., 2009, in Bohlender D. A., Durand D., Dowler P., eds, ASP Conf. Ser. Vol. 411, Astronomical Data Analysis Software and Systems XVIII. Astron. Soc. Pac., San Francisco, p. 251
Morganti R. et al., 2006, MNRAS, 371, 157
Naab T., Jesseit R., Burkert A., 2006, MNRAS, 372, 839
Naab T., Khochfar S., Burkert A., 2006, ApJ, 636, L81
Naab T., Johansson P. H., Ostriker J. P., Efstathiou G., 2007, ApJ, 658, 710
Oosterloo T. A., Morganti R., Sadler E. M., Vergani D., Caldwell N., 2002, AJ, 123, 729
Oosterloo T. et al., 2010, MNRAS, 409, 500
Padilla N. D., Strauss M. A., 2008, MNRAS, 388, 1321
Press W. H., Teukolsky S. A., Vetterling W. T., Flannery B. P., 1992, Numerical Recipes in FORTRAN. The Art of Scientific Computing, 2nd edn. Cambridge Univ. Press, Cambridge
Proctor R. N., Forbes D. A., Romanowsky A. J., Brodie J. P., Strader J., Spolaor M., Mendel J. T., Spitler L., 2009, MNRAS, 398, 91
Rix H.-W., Franx M., Fisher D., Illingworth G., 1992, ApJ, 400, L5
Rubin V. C., Graham J. A., Kenney J. D. P., 1992, ApJ, 394, L9
Ryden B. S., Terndrup D. M., Pogge R. W., Lauer T. R., 1999, ApJ, 517, 650
Sandage A., 1961, The Hubble Atlas of Galaxies. Carnegie Institution, Washington
Sarzi M. et al., 2006, MNRAS, 366, 1151
Schechter P. L., Gunn J. E., 1979, ApJ, 229, 472
Schoenmakers R. H. M., Franx M., de Zeeuw P. T., 1997, MNRAS, 292, 349
Schwarzschild M., 1982, ApJ, 263, 599
Serra P., Trager S. C., Oosterloo T. A., Morganti R., 2008, A&A, 483, 57
Stark A. A., 1977, ApJ, 213, 368
Statler T. S., 1987, ApJ, 321, 113
Statler T. S., 1991, AJ, 102, 882
Staveley-Smith L., Bland J., Axon D. J., Davies R. D., Sharples R. M., 1990, ApJ, 364, 23
Turnbull A. J., Bridges T. J., Carter D., 1999, MNRAS, 307, 967
van Albada T. S., Kotanyi C. G., Schwarzschild M., 1982, MNRAS, 198, 303
van den Bosch F. C., Abel T., Croft R. A. C., Hernquist L., White S. D. M., 2002, ApJ, 576, 21
van den Bosch R. C. E., van de Ven G., 2009, MNRAS, 398, 1117
van den Bosch R. C. E., van de Ven G., Verolme E. K., Cappellari M., de Zeeuw P. T., 2008, MNRAS, 385, 647

van der Marel R. P., Franx M., 1993, ApJ, 407, 525
Wagner S. J., Bender R., Moellenhoff C., 1988, A&A, 195, L5
Wong T., Blitz L., Bosma A., 2004, ApJ, 605, 183
Young L. M., Bureau M., Cappellari M., 2008, ApJ, 676, 317

APPENDIX A: KINEMETRIC ANALYSIS

When using the kinemetric analysis, one has to be aware of the instrumental and method-related sources of systematic errors. An in-depth description of the method and its application on velocity maps of early-type galaxies are presented in Krajnović et al. (2006, 2008). Here, we briefly review the main sources of systematic errors. The instrumental effects come from the spatial coverage, or the size of the FoV, and the spatial resolution. They particularly influence the recognition of the large- and small-scale kinematic structures. The SAURON pixel scale is 0.8 arcsec with a typical seeing of 1.5 arcsec (full width at half-maximum) and the nuclear structures of comparable sizes are not likely to be detected. This, in particular, affects KDC, CRC and 2M kinematic features. For example, observations with the OASIS, an IFS with a higher spatial resolution, showed that the nuclear regions of NGC 4150 and 4621 actually contain small CRCs (McDermid et al. 2006).

On the other hand, for some galaxies, the FoV of our observations did not cover fully one effective radius. It is possible that a full coverage (up to $1R_e$) of some galaxies would reveal, more generally, a different type of rotation or, more specifically, a certain kinematic feature. For example, NGC 3607 or 4278 is classified as a RR galaxy, but having a full $1R_e$ coverage one may characterize them as NRR/KDC galaxies.

The effects intrinsic to a kinematric analysis are related to the assumption that a velocity map is an odd moment of the LOSVD or, in other words, that there is a detectable rotation and that there are receding and approaching parts of the map. In order to constrain the parameters of the best-fitting ellipse (Γ_{kin} and q), it is necessary that the velocity map resembles to some extent the classical spider diagram. If there is no rotation, if the velocity map is noisy, in the sense that there is a large variation in the velocity between adjacent bins, and if the map is described by the cylindrical rotation (parallel isovelocities), Γ_{kin} and/or q will not be determined robustly, either becoming fully degenerate or just poorly determined. A particular consequence of this is that disc galaxies seen face-on (at an inclination of nearly 0°) could be misclassified as having the NRR type of rotation and, especially, as NRR/LV galaxies. Systems with stellar discs and a significant amount of dust could be particularly susceptible to this problem. They, however, are rare in our sample. Indeed, there is evidence that only three galaxies (NGC 3073, 4733 and 6703) might be misclassified in this way.

During the characterization of kinematic features, we strictly followed the prescription given in Sections 3.2.1 and 3.2.2 and we did not correct afterwards for the possible misclassifications mentioned above. We estimate that the largest relative contamination is indeed in the case of LV features, simply because of their low number. If the three galaxies from above are removed from group a, there would be only four (1.5 per cent) non-rotators, making these objects even more rare in the local Universe.

APPENDIX B: REMARKS ON THE DIFFERENCES BETWEEN 2M, KDC, 2σ AND CRC GALAXIES

There are two pairs of kinematic features which deserve more attention, especially in terms of the differentiation between them. They are 2M and KDC, and 2σ and CRC. The velocity maps with the 2M feature could be considered consisting of a kinematically distinct component in the central region (core) and an outer component, suggesting that they are actually a subclass of KDCs that happen to be aligned and show the RR-type rotation. They are, however, significantly different from the true KDC features. First, if they would be a subclass of KDCs, then it can be expected that there should be approximately the same number of 2M and CRC galaxies (CRCs are also a subclass of KDCs which are misaligned for 180° and hence a direct opposite to 2M). This is not true since there are 36 2M and seven CRC galaxies. In addition, more than half of 2M galaxies (20) occur in galaxies with bar and/or ring phenomena, which is not the case for KDC and CRC features. This indicates that the formation scenario is different for 2M and KDC galaxies.

Unlike all other kinematic features, 2σ galaxies are recognized by looking at the velocity dispersion maps. The reason is that the velocity maps of galaxies with this feature have various appearances. The most common feature in the velocity maps are counter-rotating components (e.g. NGC 448), but it is possible to have multiple sign reversals (e.g. NGC 4528) or ordered RR rotation (e.g. NGC 4473) or even no rotation in the central region (e.g. NGC 4550). The two peaks in the velocity dispersion maps, which are aligned and occur on the major-axis of the galaxies, are, however, always present. The velocity dispersion maps of, for example, galaxies with the CRC features show a central increase in σ (see Fig. B1 for a comparison) and, most likely, CRC and 2σ galaxies have different formation scenarios.

There is compelling evidence that the 2σ peaks are signatures of two counter-rotating disc-like structures. The most famous example of these galaxies is NGC 4550 which was shown to consist of two equal-mass stellar discs with opposite angular momenta, both by studying the shape of the LOSVD (Rix et al. 1992; Rubin, Graham & Kenney 1992) and by constructing dynamical models (Cappellari et al. 2007). The latter study also showed that NGC 4733, a 2σ galaxy which does not show evidence of a counter-rotation in the velocity map, also consists of two components with opposite angular momenta. A similar configuration would also be the simplest explanation for the consecutive changes in the velocity
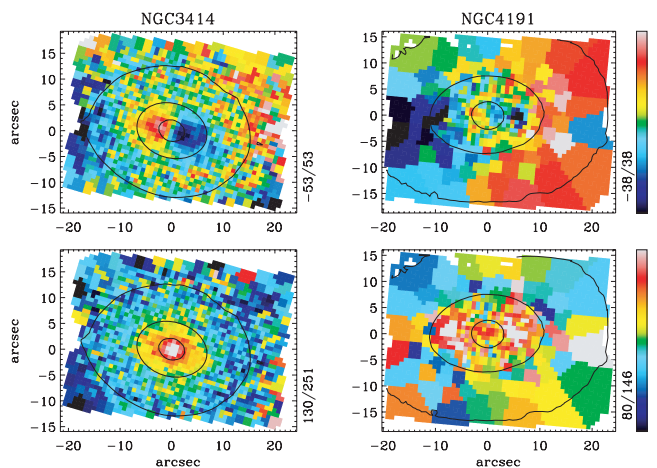
Figure B1. The mean velocity (top panels) and the velocity dispersion maps (bottom panels) for NGC 3414 (left-hand column) and NGC 4191 (right-hand column). These galaxies have similar apparent shapes (0.23 and 0.27, respectively) and both have counter-rotating components in the velocity maps. Their velocity dispersion maps are very different and NGC 3414 is classified as a NRR/CRC galaxy, while NGC 4191 is classified as a NRR/2σ galaxy.
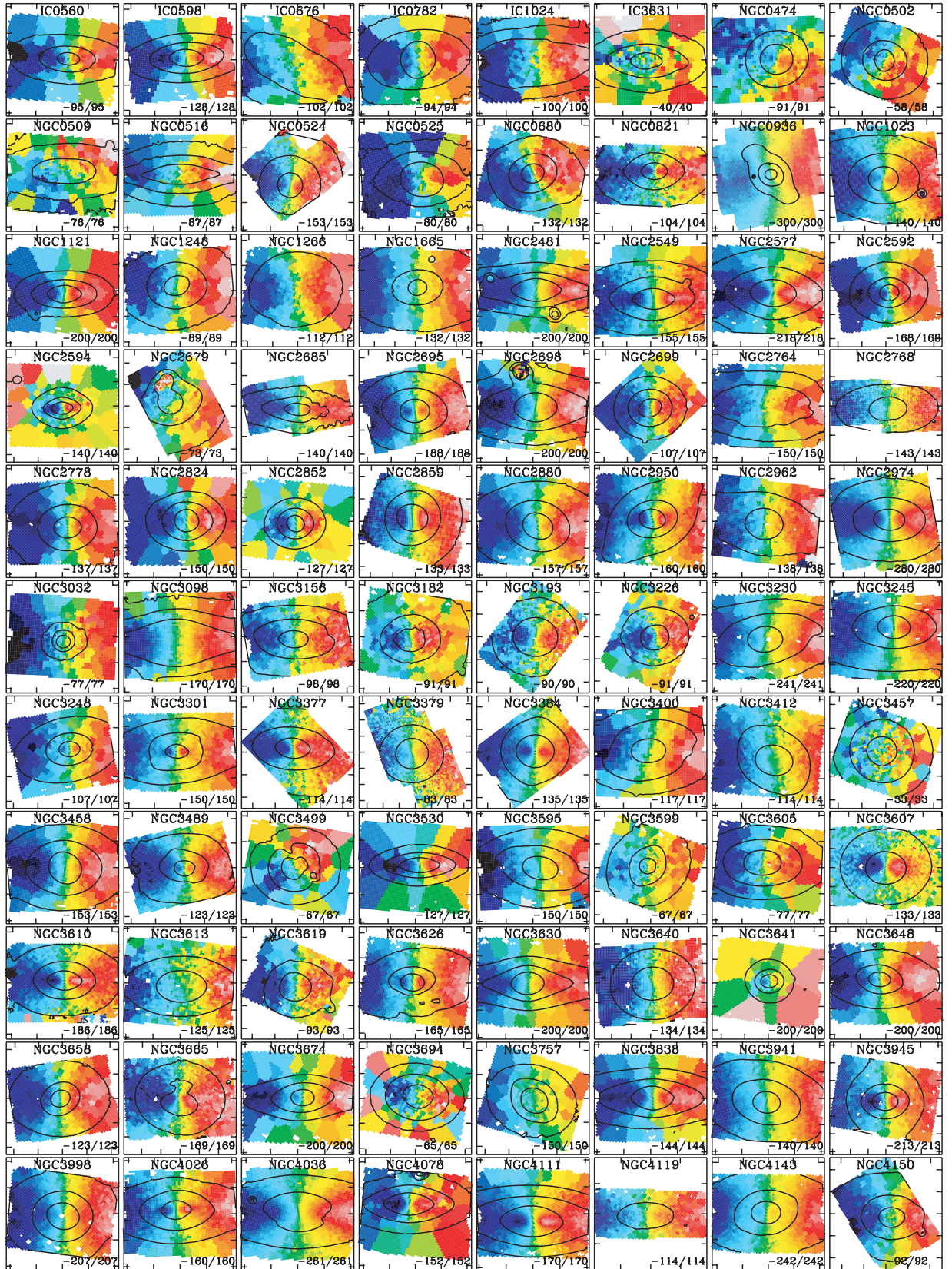
Figure C1. Velocity maps of galaxies of kinematic group e (RR). Contours are isphotes of the surface brightness. Maps are Voronoi binned (Cappellari & Copin 2003). All galaxies are oriented such that the global photometric axis (PA_{phot}) is horizontal and that the receding part is on the right-hand side. The numbers in the lower right-hand corners show the range of the plotted velocities in km s^{-1}. Ticks are separated by 10 arcsec. Figures with maps oriented – north towards up and east to the left – are available at the project website: http://purl.org/atlas3d. Galaxies with an 'F' were not classified but are plotted here for completeness.
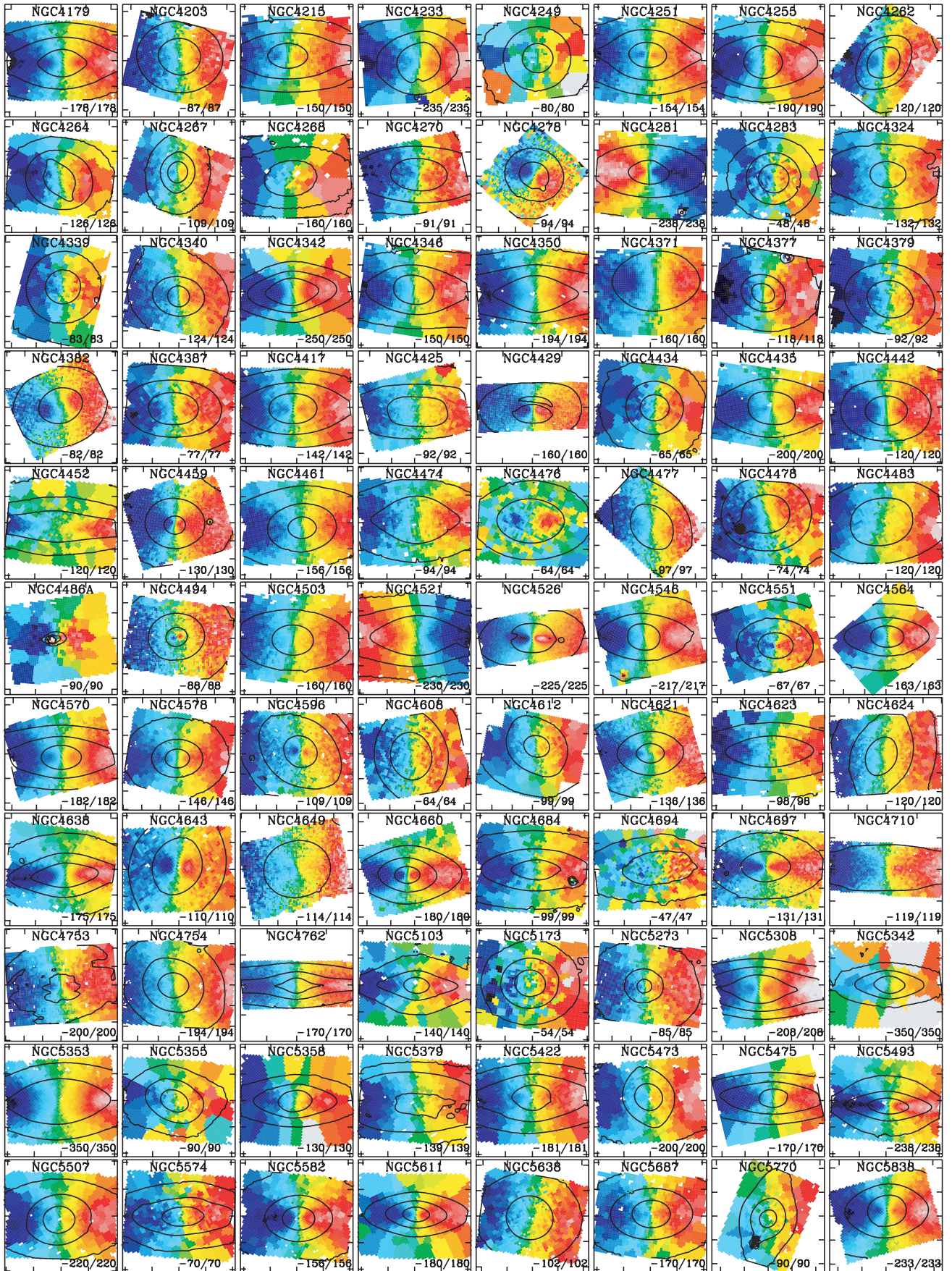
Figure C1 – *continued*
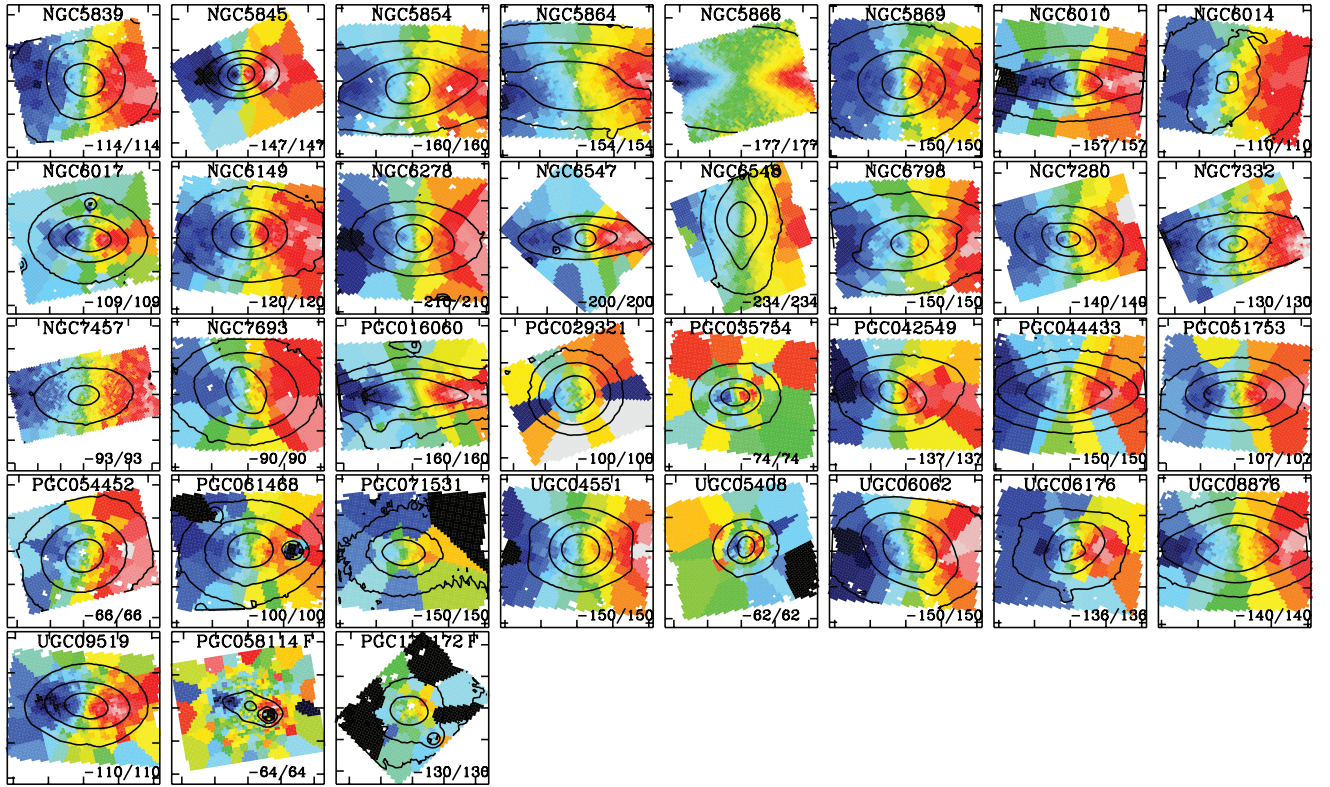
Figure C1 – *continued*

sign in NGC 4528, as well as to explain why 2σ galaxies have both the RR and NRR types of rotation.

Most of the 2σ galaxies are flattened systems seen at high viewing angles, which introduces a bias since decreasing the inclination also dilutes the signature in the velocity dispersion maps [but see Paper VI for maps of 2σ galaxies at various inclinations], and their frequency of 4 per cent is likely just a lower limit. In addition, we choose to identify objects with substantial mass in the counter-rotating discs, which is reflected in the increasing separation between the 2σ peaks. There are a few galaxies which show some signatures of 2σ peaks (e.g. NGC 661, 4150 and 7332), but they are not resolved well in SAURON velocity dispersion maps.

APPENDIX C: THE MEAN VELOCITY MAPS OF ATLAS[3D] GALAXIES
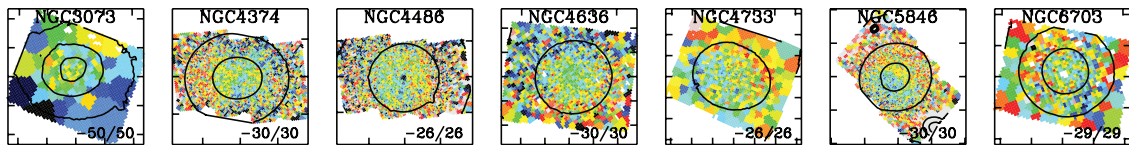
Figure C2. Same as in Fig. C1, but for galaxies of kinematic group a (non-rotating galaxies).
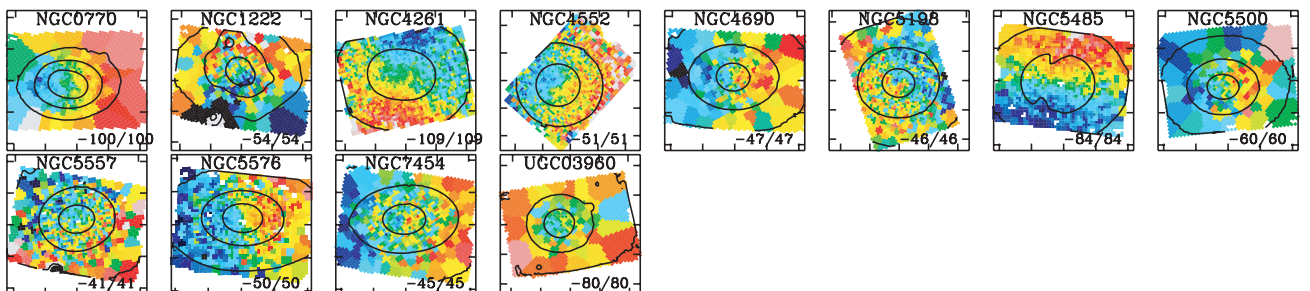
Figure C3. Same as in Fig. C1, but for galaxies of kinematic group b (featureless NRR galaxies).
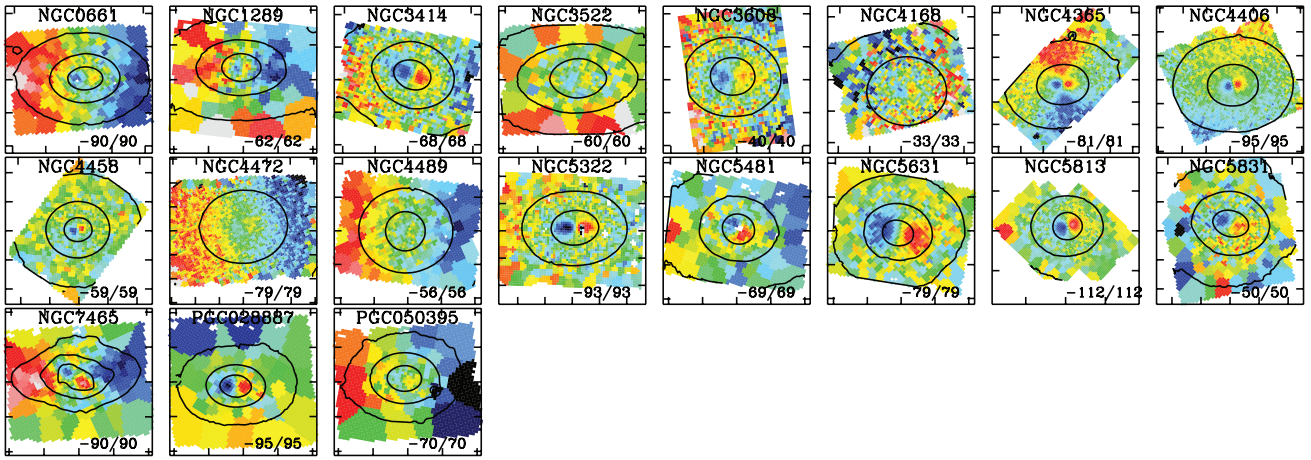
Figure C4. Same as in Fig. C1, but for galaxies of kinematic group c (KDC and CRC galaxies). Galaxies are oriented such that the receding part of the KDC is on the right-hand side.
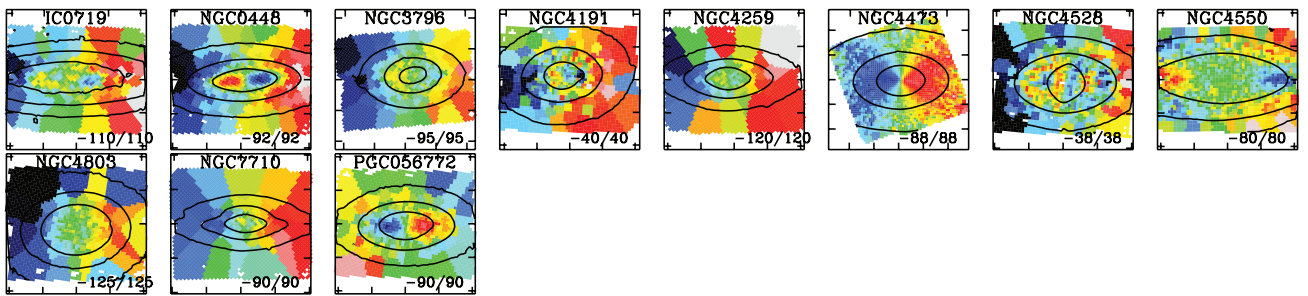
Figure C5. Same as in Fig. C1, but for galaxies of kinematic group d (2σ peak galaxies).
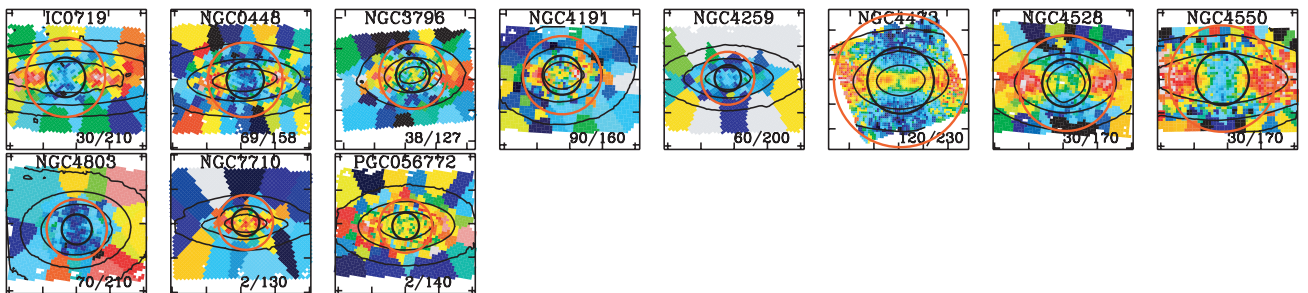
Figure C6. The velocity dispersion maps of galaxies of kinematic group d (as in Fig. C5). Note two aligned peaks in the velocity dispersion which are separated by at least half of the effective radius. The overplotted circles show one and a half effective radii. The numbers in the lower right-hand corners show the range of the plotted velocity dispersions in km s^{-1}.

APPENDIX D: TABLE WITH MAIN PROPERTIES OF ATLAS³ᴰ GALAXIES USED IN THIS PAPER

Table D1. Properties of ATLAS³ᴰ galaxies.

Name	PA_{phot} (°)	ϵ	PA_{kin} (°)	Ψ (°)	$\overline{k_5/k_1}$	k_1^{max} (km s^{-1})	Morphological property	Dust feature	Kinematic structure	Group
(1)	(2)	(3)	(4)	(5)	(6)	(7)	(8)	(9)	(10)	(11)
IC 0560	18.0 ± 4.1	0.56 ± 0.20	17.0 ± 8.2	1.0	0.036 ± 0.024	75.0	N	N	RR/NF	e
IC 0598	4.5 ± 1.4	0.67 ± 0.02	6.5 ± 4.5	2.0	0.026 ± 0.017	108.4	N	N	RR/NF	e
IC 0676	5.9 ± 77.2	0.25 ± 0.09	18.5 ± 12.2	12.6	0.034 ± 0.045	82.3	BR	F	RR/NF	e
IC 0719	51.9 ± 0.1	0.71 ± 0.01	46.0 ± 26.8	5.9	0.294 ± 0.129	26.9	N	D	NRR/2s	d
IC 0782	58.1 ± 2.8	0.28 ± 0.06	242.5 ± 9.2	4.4	0.028 ± 0.022	73.7	BR	N	RR/NF	e
IC 1024	26.9 ± 0.7	0.64 ± 0.06	29.5 ± 10.8	2.6	0.049 ± 0.036	71.6	I	F	RR/NF	e
IC 3631	89.1 ± 0.7	0.43 ± 0.04	79.0 ± 89.8	10.1	0.155 ± 0.151	15.1	N	B	RR/NF	e
NGC 0448	114.2 ± 0.2	0.57 ± 0.06	119.0 ± 2.8	4.8	0.050 ± 0.020	72.0	N	N	RR/2s	d
NGC 0474	177.8 ± 7.9	0.12 ± 0.06	326.5 ± 7.5	31.3	0.063 ± 0.022	70.9	S	N	RR/KT	e
NGC 0502	50.2 ± 17.0	0.10 ± 0.03	193.0 ± 13.8	37.2	0.062 ± 0.039	38.0	B	N	RR/NF	e
NGC 0509	82.7 ± 2.2	0.64 ± 0.07	130.5 ± 16.0	47.8	0.094 ± 0.064	56.3	B	N	RR/NF	e
NGC 0516	43.9 ± 0.6	0.66 ± 0.09	222.0 ± 16.0	1.9	0.051 ± 0.046	66.6	N	N	RR/NF	e
NGC 0524	47.4 ± 25.5	0.05 ± 0.03	40.5 ± 2.0	6.9	0.021 ± 0.008	133.0	N	N	RR/NF	e
NGC 0525	7.9 ± 1.7	0.47 ± 0.05	14.0 ± 15.2	6.1	0.049 ± 0.031	59.6	N	N	RR/NF	e
NGC 0661	54.2 ± 3.5	0.31 ± 0.01	236.0 ± 12.0	1.8	0.186 ± 0.063	41.3	N	N	NRR/CRC	c
NGC 0680	156.8 ± 5.2	0.22 ± 0.01	359.5 ± 3.8	22.7	0.028 ± 0.010	111.6	S	N	RR/NF	e
NGC 0770	12.5 ± 1.4	0.29 ± 0.01	194.5 ± 11.8	2.0	0.124 ± 0.042	41.9	N	N	NRR/NF	b
NGC 0821	31.2 ± 13.6	0.35 ± 0.10	32.5 ± 3.5	1.3	0.017 ± 0.008	83.7	N	N	RR/NF	e
NGC 0936	130.7 ± 1.3	0.22 ± 0.01	318.0 ± 0.5	7.3	0.038 ± 0.006	203.6	B	N	RR/2m	e
NGC 1023	83.3 ± 2.8	0.63 ± 0.03	88.5 ± 2.2	5.2	0.018 ± 0.006	119.8	B	N	RR/NF	e
NGC 1121	10.1 ± 0.3	0.51 ± 0.04	9.0 ± 3.8	1.1	0.015 ± 0.009	157.7	N	N	RR/NF	e
NGC 1222	150.3 ± 12.0	0.28 ± 0.08	43.0 ± 9.2	72.7	0.239 ± 0.153	34.1	I	F	NRR/NF	b
NGC 1248	99.9 ± 0.8	0.15 ± 0.01	275.5 ± 9.5	4.4	0.034 ± 0.027	69.5	B	N	RR/NF	e
NGC 1266	109.6 ± 1.9	0.25 ± 0.04	294.5 ± 7.0	4.9	0.026 ± 0.022	92.4	N	F	RR/NF	e
NGC 1289	96.6 ± 3.2	0.41 ± 0.02	92.0 ± 10.0	4.6	0.176 ± 0.056	42.0	N	N	NRR/CRC	c
NGC 1665	47.3 ± 16.9	0.41 ± 0.21	48.0 ± 8.5	0.7	0.042 ± 0.025	112.1	R	N	RR/NF	e
NGC 2481	20.2 ± 16.1	0.46 ± 0.17	19.5 ± 2.0	0.7	0.016 ± 0.007	152.5	N	N	RR/NF	e
NGC 2549	179.5 ± 1.0	0.69 ± 0.03	2.0 ± 1.8	2.5	0.029 ± 0.006	134.5	BR	N	RR/2m	e
NGC 2577	105.9 ± 3.8	0.41 ± 0.12	104.0 ± 2.0	1.9	0.010 ± 0.005	198.5	N	N	RR/NF	e
NGC 2592	49.4 ± 4.8	0.21 ± 0.01	58.5 ± 3.2	9.1	0.014 ± 0.008	148.0	N	N	RR/NF	e
NGC 2594	30.2 ± 7.3	0.32 ± 0.05	34.0 ± 4.5	3.8	0.020 ± 0.009	119.7	N	N	RR/NF	e
NGC 2679	151.0 ± 7.8	0.07 ± 0.06	307.5 ± 17.5	23.5	0.061 ± 0.047	53.4	BR	N	RR/NF	e
NGC 2685	39.0 ± 2.5	0.40 ± 0.05	36.5 ± 2.5	2.5	0.018 ± 0.010	109.4	N	F	RR/NF	e
NGC 2695	172.5 ± 1.6	0.28 ± 0.01	173.5 ± 2.2	1.0	0.016 ± 0.006	168.3	N	N	RR/2m	e
NGC 2698	97.1 ± 7.7	0.54 ± 0.25	95.5 ± 2.0	1.6	0.014 ± 0.007	169.3	N	N	RR/NF	e
NGC 2699	46.8 ± 4.7	0.14 ± 0.03	230.0 ± 4.8	3.2	0.027 ± 0.013	87.3	N	N	RR/2m	e
NGC 2764	19.2 ± 3.2	0.49 ± 0.11	196.0 ± 6.8	3.2	0.025 ± 0.021	103.8	I	FB	RR/NF	e
NGC 2768	91.6 ± 2.1	0.57 ± 0.06	92.5 ± 3.5	0.9	0.034 ± 0.011	122.9	N	N	RR/NF	e
NGC 2778	44.3 ± 6.2	0.20 ± 0.02	45.5 ± 4.8	1.2	0.038 ± 0.012	117.2	N	N	RR/NF	e
NGC 2824	158.9 ± 7.7	0.24 ± 0.10	159.5 ± 2.8	0.6	0.029 ± 0.013	109.2	R	D	RR/NF	e
NGC 2852	154.3 ± 2.4	0.14 ± 0.01	156.0 ± 4.8	1.7	0.015 ± 0.013	107.0	N	N	RR/NF	e
NGC 2859	87.2 ± 37.4	0.15 ± 0.01	264.0 ± 3.0	3.2	0.016 ± 0.006	113.4	BR	N	RR/2m	e
NGC 2880	142.5 ± 1.7	0.36 ± 0.01	143.0 ± 3.2	0.5	0.023 ± 0.010	136.8	B	N	RR/NF	e
NGC 2950	118.1 ± 3.5	0.41 ± 0.03	114.0 ± 3.2	4.1	0.013 ± 0.007	133.1	BR	N	RR/2m	e
NGC 2962	6.1 ± 3.4	0.45 ± 0.04	8.0 ± 5.5	1.9	0.041 ± 0.016	117.7	BR	N	RR/NF	e
NGC 2974	44.2 ± 5.5	0.37 ± 0.03	43.0 ± 1.0	1.2	0.007 ± 0.003	231.1	N	N	RR/NF	e
NGC 3032	92.3 ± 21.6	0.17 ± 0.10	271.5 ± 11.0	0.8	0.038 ± 0.027	56.5	N	DB	RR/NF	e
NGC 3073	145.0 ± 30.4	0.12 ± 0.01	215.0 ± 89.8	70.0	0.405 ± 0.307	6.4	N	B	NRR/LV	a
NGC 3098	88.5 ± 0.4	0.77 ± 0.04	269.0 ± 3.0	0.5	0.021 ± 0.010	122.1	N	N	RR/NF	e
NGC 3156	50.1 ± 1.0	0.50 ± 0.01	48.5 ± 5.5	1.6	0.028 ± 0.023	78.3	N	F	RR/NF	e

Table D1 – *continued*

Name	PA$_{phot}$ (°)	ϵ	PA$_{kin}$ (°)	Ψ (°)	$\overline{k_5/k_1}$	k_1^{max} (km s^{-1})	Morphological property	Dust feature	Kinematic structure	Group
(1)	(2)	(3)	(4)	(5)	(6)	(7)	(8)	(9)	(10)	(11)
NGC 3182	136.8 ± 5.2	0.20 ± 0.02	320.5 ± 7.0	3.7	0.054 ± 0.024	70.5	N	BR	RR/NF	e
NGC 3193	5.9 ± 19.6	0.09 ± 0.02	181.0 ± 4.5	4.9	0.047 ± 0.014	69.6	N	N	RR/NF	e
NGC 3226	34.9 ± 12.1	0.17 ± 0.05	44.0 ± 6.2	9.1	0.050 ± 0.020	71.3	I	N	RR/NF	e
NGC 3230	112.8 ± 0.5	0.61 ± 0.03	289.5 ± 3.2	3.3	0.028 ± 0.009	221.3	BR	N	RR/NF	e
NGC 3245	176.1 ± 0.6	0.46 ± 0.03	174.5 ± 3.0	1.6	0.015 ± 0.006	181.3	N	N	RR/NF	e
NGC 3248	123.4 ± 6.0	0.40 ± 0.01	122.0 ± 9.0	1.4	0.043 ± 0.023	87.4	R	N	RR/2m	e
NGC 3301	52.7 ± 0.5	0.69 ± 0.01	229.0 ± 4.0	3.7	0.028 ± 0.012	118.0	R	N	RR/2m	e
NGC 3377	46.3 ± 8.2	0.33 ± 0.12	224.0 ± 4.0	2.3	0.013 ± 0.008	93.7	N	N	RR/NF	e
NGC 3379	68.2 ± 2.3	0.13 ± 0.01	251.0 ± 5.2	2.8	0.022 ± 0.010	62.7	N	N	RR/NF	e
NGC 3384	53.0 ± 1.9	0.50 ± 0.03	228.0 ± 3.2	5.0	0.018 ± 0.006	114.9	B	N	RR/2m	e
NGC 3400	91.4 ± 2.5	0.44 ± 0.01	77.0 ± 8.8	14.4	0.026 ± 0.027	97.2	BR	N	RR/NF	e
NGC 3412	154.0 ± 0.3	0.44 ± 0.01	157.5 ± 5.8	3.5	0.026 ± 0.016	93.8	B	N	RR/NF	e
NGC 3414	19.4 ± 2.2	0.22 ± 0.06	197.5 ± 7.5	1.9	0.159 ± 0.051	47.5	I	N	NRR/CRC	c
NGC 3457	162.5 ± 10.4	0.01 ± 0.01	334.0 ± 38.2	8.5	0.157 ± 0.124	13.1	N	N	RR/NF	e
NGC 3458	7.1 ± 0.9	0.29 ± 0.02	185.5 ± 3.5	1.6	0.018 ± 0.010	132.5	B	N	RR/NF	e
NGC 3489	70.5 ± 1.3	0.45 ± 0.04	72.5 ± 2.8	2.0	0.022 ± 0.010	103.0	B	DBR	RR/NF	e
NGC 3499	11.6 ± 2.2	0.13 ± 0.16	50.0 ± 12.0	38.4	0.054 ± 0.046	46.6	I	F	RR/NF	e
NGC 3522	113.3 ± 0.5	0.48 ± 0.03	113.5 ± 89.8	0.2	0.229 ± 0.170	19.2	N	N	NRR/KDC	c
NGC 3530	96.1 ± 0.4	0.53 ± 0.04	98.5 ± 4.8	2.4	0.029 ± 0.018	107.2	N	N	RR/NF	e
NGC 3595	177.6 ± 1.7	0.46 ± 0.02	0.5 ± 1.5	2.9	0.041 ± 0.018	93.4	B	N	RR/NF	e
NGC 3599	53.5 ± 17.9	0.08 ± 0.01	55.5 ± 17.2	2.0	0.087 ± 0.054	47.4	B	N	RR/NF	e
NGC 3605	19.4 ± 0.1	0.40 ± 0.13	198.0 ± 11.0	1.4	0.036 ± 0.029	57.4	S	N	RR/NF	e
NGC 3607	124.8 ± 7.6	0.13 ± 0.08	301.5 ± 2.8	3.3	0.028 ± 0.013	113.3	N	D	RR/NF	e
NGC 3608	82.0 ± 23.7	0.20 ± 0.04	265.5 ± 35.2	3.5	0.190 ± 0.102	20.0	N	N	NRR/CRC	c
NGC 3610	134.1 ± 14.9	0.19 ± 0.04	134.5 ± 0.5	0.4	0.020 ± 0.004	166.5	S	N	RR/NF	e
NGC 3613	97.5 ± 1.1	0.46 ± 0.04	98.5 ± 3.8	1.0	−1.000 ± −1.000	105.4	N	N	RR/NF	e
NGC 3619	48.6 ± 12.4	0.09 ± 0.08	52.5 ± 3.0	3.9	0.058 ± 0.022	72.9	S	FBR	RR/NF	e
NGC 3626	161.7 ± 3.2	0.33 ± 0.05	339.5 ± 3.2	2.2	0.023 ± 0.011	145.2	R	D	RR/2m	e
NGC 3630	36.9 ± 0.2	0.66 ± 0.05	217.0 ± 2.8	0.1	0.021 ± 0.007	143.8	N	N	RR/NF	e
NGC 3640	88.5 ± 6.2	0.15 ± 0.02	271.5 ± 3.0	3.0	0.019 ± 0.009	114.2	I	N	RR/NF	e
NGC 3641	56.8 ± 18.2	0.11 ± 0.01	69.5 ± 9.0	12.7	0.066 ± 0.034	83.1	N	N	RR/NF	e
NGC 3648	72.3 ± 0.1	0.44 ± 0.03	254.5 ± 3.0	2.2	0.018 ± 0.008	173.7	N	N	RR/NF	e
NGC 3658	30.2 ± 3.6	0.16 ± 0.01	210.5 ± 4.8	0.3	0.024 ± 0.014	102.6	B	N	RR/NF	e
NGC 3665	30.9 ± 2.0	0.22 ± 0.01	205.5 ± 2.0	5.4	0.019 ± 0.008	149.2	N	D	RR/NF	e
NGC 3674	30.9 ± 0.2	0.64 ± 0.02	31.5 ± 2.5	0.6	0.034 ± 0.010	147.4	N	N	RR/2m	e
NGC 3694	117.7 ± 1.6	0.18 ± 0.04	109.0 ± 9.2	8.7	0.052 ± 0.049	45.3	N	B	RR/NF	e
NGC 3757	151.2 ± 6.9	0.15 ± 0.02	160.5 ± 15.8	9.3	−1.000 ± −1.000	28.1	BR	N	RR/NF	e
NGC 3796	124.4 ± 0.3	0.40 ± 0.01	125.5 ± 14.2	1.1	0.212 ± 0.136	23.1	B	N	NRR/2s	d
NGC 3838	139.1 ± 1.0	0.56 ± 0.04	138.5 ± 3.5	0.6	0.020 ± 0.009	124.0	N	N	RR/NF	e
NGC 3941	11.7 ± 1.4	0.25 ± 0.04	15.0 ± 3.5	3.3	0.017 ± 0.007	120.3	BR	N	RR/NF	e
NGC 3945	158.1 ± 11.7	0.35 ± 0.17	158.5 ± 2.0	0.4	0.015 ± 0.007	193.5	BR	FBR	RR/2m	e
NGC 3998	136.3 ± 4.6	0.22 ± 0.06	134.5 ± 2.0	1.8	0.012 ± 0.006	186.7	N	N	RR/NF	e
NGC 4026	177.5 ± 0.2	0.75 ± 0.02	1.5 ± 3.0	4.0	0.024 ± 0.006	139.9	N	N	RR/2m	e
NGC 4036	81.2 ± 0.9	0.60 ± 0.03	261.0 ± 1.0	0.2	0.011 ± 0.004	241.2	N	F	RR/NF	e
NGC 4078	18.3 ± 0.8	0.56 ± 0.09	192.0 ± 1.5	6.3	0.022 ± 0.008	132.2	N	N	RR/NF	e
NGC 4111	150.3 ± 0.3	0.79 ± 0.02	149.5 ± 2.2	0.8	0.031 ± 0.004	150.3	N	N	RR/2m	e
NGC 4119	111.3 ± 0.5	0.65 ± 0.01	291.5 ± 6.5	0.2	0.020 ± 0.020	93.8	N	D	RR/NF	e
NGC 4143	144.2 ± 1.1	0.40 ± 0.04	320.5 ± 2.2	3.7	0.024 ± 0.007	221.7	B	N	RR/2m	e
NGC 4150	146.3 ± 1.1	0.33 ± 0.01	147.5 ± 6.5	1.2	0.043 ± 0.024	72.3	N	N	RR/NF	e
NGC 4168	125.4 ± 2.0	0.17 ± 0.05	320.0 ± 89.8	14.6	0.343 ± 0.170	13.3	N	N	NRR/KDC	c
NGC 4179	142.8 ± 0.3	0.71 ± 0.02	143.5 ± 2.2	0.7	0.025 ± 0.006	157.9	N	N	RR/NF	e
NGC 4191	3.6 ± 2.9	0.26 ± 0.04	182.5 ± 4.8	1.1	0.424 ± 0.144	20.3	N	N	NRR/2s	d
NGC 4203	13.2 ± 2.2	0.11 ± 0.03	194.5 ± 5.8	1.3	0.030 ± 0.014	67.2	N	N	RR/NF	e
NGC 4215	174.8 ± 0.1	0.64 ± 0.01	172.0 ± 5.5	2.8	0.019 ± 0.013	101.5	BR	N	RR/2m	e
NGC 4233	175.8 ± 0.4	0.55 ± 0.01	174.5 ± 1.2	1.3	0.029 ± 0.008	200.9	N	F	RR/NF	e
NGC 4249	91.8 ± 8.8	0.05 ± 0.01	94.0 ± 25.0	2.2	0.099 ± 0.069	35.9	N	N	RR/NF	e

Table D1 – *continued*

Name	PA$_{phot}$ (°)	ϵ	PA$_{kin}$ (°)	Ψ (°)	$\overline{k_5/k_1}$	k_1^{max} (km s^{-1})	Morphological property	Dust feature	Kinematic structure	Group
(1)	(2)	(3)	(4)	(5)	(6)	(7)	(8)	(9)	(10)	(11)
NGC 4251	99.0 ± 0.9	0.48 ± 0.05	277.5 ± 3.0	1.5	0.022 ± 0.008	134.3	B	N	RR/2m	e
NGC 4255	111.5 ± 0.2	0.49 ± 0.06	111.0 ± 3.2	0.5	0.019 ± 0.009	157.7	B	N	RR/NF	e
NGC 4259	142.7 ± 0.5	0.58 ± 0.03	146.0 ± 6.2	3.3	0.289 ± 0.176	39.7	N	N	NRR/2s	d
NGC 4261	163.3 ± 1.9	0.16 ± 0.03	57.0 ± 2.5	73.7	0.087 ± 0.029	88.6	N	N	NRR/NF	b
NGC 4262	156.6 ± 1.6	0.12 ± 0.01	329.0 ± 3.5	7.6	0.025 ± 0.008	86.7	BR	N	RR/2m	e
NGC 4264	119.8 ± 5.5	0.19 ± 0.01	118.0 ± 5.5	1.8	0.050 ± 0.012	105.9	BR	N	RR/NF	e
NGC 4267	126.5 ± 5.6	0.08 ± 0.01	304.5 ± 6.5	2.0	0.043 ± 0.015	88.7	B	N	RR/2m	e
NGC 4268	47.3 ± 1.3	0.55 ± 0.04	25.0 ± 16.8	22.3	0.063 ± 0.032	121.5	R	N	RR/NF	e
NGC 4270	109.8 ± 1.5	0.55 ± 0.04	282.5 ± 7.0	7.3	0.041 ± 0.016	70.9	S	N	RR/NF	e
NGC 4278	39.5 ± 2.8	0.09 ± 0.01	10.0 ± 4.2	29.5	0.035 ± 0.016	74.2	N	N	RR/NF	e
NGC 4281	87.6 ± 1.0	0.51 ± 0.04	85.0 ± 1.5	2.6	0.010 ± 0.004	217.8	N	D	RR/NF	e
NGC 4283	153.1 ± 14.7	0.04 ± 0.01	151.5 ± 16.5	1.6	0.055 ± 0.038	27.8	N	N	RR/NF	e
NGC 4324	54.2 ± 1.0	0.56 ± 0.03	238.0 ± 5.2	3.8	0.042 ± 0.018	111.6	R	DBR	RR/2m	e
NGC 4339	15.7 ± 8.2	0.07 ± 0.01	17.0 ± 10.8	1.3	0.044 ± 0.030	63.0	N	N	RR/NF	e
NGC 4340	104.9 ± 9.9	0.42 ± 0.08	110.0 ± 5.0	5.1	0.022 ± 0.016	103.7	BR	N	RR/NF	e
NGC 4342	163.6 ± 1.5	0.58 ± 0.09	167.0 ± 1.8	3.4	0.010 ± 0.005	168.2	N	N	RR/NF	e
NGC 4346	98.8 ± 0.2	0.64 ± 0.02	280.0 ± 3.5	1.2	0.020 ± 0.010	130.0	N	N	RR/NF	e
NGC 4350	28.4 ± 0.5	0.60 ± 0.12	29.5 ± 2.2	1.1	0.014 ± 0.006	174.2	N	N	RR/NF	e
NGC 4365	40.9 ± 2.1	0.24 ± 0.02	145.0 ± 6.5	75.9	0.347 ± 0.067	60.9	N	N	NRR/KDC	c
NGC 4371	91.5 ± 4.1	0.48 ± 0.10	270.5 ± 3.0	1.0	0.022 ± 0.009	124.4	BR	N	RR/NF	e
NGC 4374	128.8 ± 9.3	0.05 ± 0.01	351.5 ± 89.5	42.7	0.566 ± 0.182	10.4	N	N	NRR/LV	a
NGC 4377	4.0 ± 2.2	0.18 ± 0.02	0.5 ± 5.0	3.5	0.037 ± 0.016	97.9	R	N	RR/NF	e
NGC 4379	104.9 ± 1.7	0.16 ± 0.00	283.5 ± 7.8	1.4	0.039 ± 0.022	72.0	N	N	RR/NF	e
NGC 4382	12.3 ± 11.0	0.25 ± 0.07	19.5 ± 4.8	7.2	0.025 ± 0.009	61.8	S	N	RR/KT	e
NGC 4387	143.4 ± 2.1	0.37 ± 0.03	331.0 ± 1.0	7.6	0.029 ± 0.022	57.1	N	N	RR/NF	e
NGC 4406	118.1 ± 3.7	0.31 ± 0.06	199.5 ± 12.0	81.4	0.097 ± 0.024	67.3	N	N	NRR/KDC	c
NGC 4417	48.6 ± 0.5	0.65 ± 0.09	228.0 ± 4.2	0.6	0.020 ± 0.010	121.8	N	N	RR/2m	e
NGC 4425	25.8 ± 0.4	0.67 ± 0.04	210.0 ± 8.2	4.2	0.044 ± 0.029	72.0	B	N	RR/NF	e
NGC 4429	93.3 ± 1.6	0.52 ± 0.04	86.5 ± 2.5	6.8	0.021 ± 0.006	139.6	BR	D	RR/2m	e
NGC 4434	34.7 ± 7.1	0.06 ± 0.01	207.0 ± 11.5	7.7	0.060 ± 0.040	44.6	N	N	RR/NF	e
NGC 4435	10.0 ± 2.0	0.32 ± 0.05	192.5 ± 1.8	2.5	0.020 ± 0.006	162.3	N	D	RR/2m	e
NGC 4442	85.6 ± 0.2	0.60 ± 0.00	90.5 ± 3.0	4.9	0.018 ± 0.007	99.7	B	N	RR/NF	e
NGC 4452	33.6 ± 1.7	0.73 ± 0.04	30.5 ± 3.0	3.1	−1.000 ± −1.000	80.1	N	N	RR/NF	e
NGC 4458	4.9 ± 3.5	0.08 ± 0.02	25.0 ± 29.2	20.1	0.374 ± 0.172	39.4	N	N	NRR/KDC	c
NGC 4459	105.3 ± 1.9	0.21 ± 0.03	280.5 ± 2.5	4.8	0.010 ± 0.007	110.2	N	D	RR/2m	e
NGC 4461	8.1 ± 0.4	0.61 ± 0.01	11.5 ± 3.2	3.4	0.023 ± 0.010	136.3	BR	N	RR/NF	e
NGC 4472	154.7 ± 4.6	0.19 ± 0.03	169.0 ± 5.5	14.3	0.197 ± 0.075	58.9	N	N	NRR/CRC	c
NGC 4473	92.2 ± 1.2	0.43 ± 0.03	92.0 ± 3.8	0.2	0.062 ± 0.010	68.2	N	N	NRR/2s	d
NGC 4474	79.4 ± 2.2	0.42 ± 0.16	79.0 ± 6.8	0.4	0.061 ± 0.027	74.4	N	N	RR/NF	e
NGC 4476	26.7 ± 2.6	0.28 ± 0.03	206.5 ± 11.5	0.2	0.102 ± 0.065	43.9	N	D	RR/NF	e
NGC 4477	70.8 ± 8.9	0.14 ± 0.01	252.5 ± 5.2	1.7	0.023 ± 0.011	77.1	BR	N	RR/NF	e
NGC 4478	141.9 ± 8.7	0.17 ± 0.01	156.5 ± 6.5	14.6	0.039 ± 0.015	54.3	N	N	RR/NF	e
NGC 4483	62.5 ± 1.3	0.51 ± 0.04	231.5 ± 8.5	11.0	0.032 ± 0.025	87.5	BR	N	RR/NF	e
NGC 4486	151.3 ± 3.5	0.16 ± 0.06	197.5 ± 57.8	46.2	0.484 ± 0.197	5.9	N	N	NRR/LV	a
NGC 4486A	5.4 ± 0.5	0.15 ± 0.01	6.0 ± 8.5	0.6	0.031 ± 0.020	75.8	N	N	RR/NF	e
NGC 4489	155.6 ± 1.1	0.09 ± 0.00	156.5 ± 30.5	0.9	0.063 ± 0.121	36.1	N	N	RR/CRC	c
NGC 4494	176.3 ± 2.1	0.14 ± 0.02	185.0 ± 6.0	8.7	0.054 ± 0.024	68.1	N	N	RR/2m	e
NGC 4503	8.7 ± 1.4	0.54 ± 0.02	183.0 ± 4.5	5.7	0.021 ± 0.011	140.3	BR	N	RR/NF	e
NGC 4521	166.3 ± 0.2	0.73 ± 0.01	349.0 ± 2.8	2.7	0.013 ± 0.006	195.7	N	N	RR/NF	e
NGC 4526	113.7 ± 1.2	0.76 ± 0.05	288.5 ± 1.8	5.2	0.024 ± 0.003	205.0	N	D	RR/2m	e
NGC 4528	5.8 ± 0.8	0.41 ± 0.02	5.0 ± 11.0	0.8	1.025 ± 0.250	18.1	B	N	NRR/2s	d
NGC 4546	77.8 ± 1.9	0.52 ± 0.04	77.5 ± 1.5	0.3	0.010 ± 0.004	197.0	N	N	RR/NF	e
NGC 4550	178.9 ± 0.4	0.68 ± 0.01	358.5 ± 2.5	0.4	0.396 ± 0.217	13.2	N	N	NRR/2s	d
NGC 4551	70.5 ± 1.0	0.25 ± 0.02	247.0 ± 10.0	3.5	0.034 ± 0.023	47.2	N	N	RR/NF	e
NGC 4552	132.0 ± 1.2	0.11 ± 0.01	119.5 ± 5.2	12.5	0.081 ± 0.035	30.5	N	N	NRR/NF	b
NGC 4564	48.5 ± 0.3	0.53 ± 0.04	49.0 ± 2.8	0.5	0.013 ± 0.007	142.8	N	N	RR/NF	e

Table D1 – *continued*

Name	PA$_{phot}$ (°)	ϵ	PA$_{kin}$ (°)	Ψ (°)	$\overline{k_5/k_1}$	k_1^{max} (km s^{-1})	Morphological property	Dust feature	Kinematic structure	Group
(1)	(2)	(3)	(4)	(5)	(6)	(7)	(8)	(9)	(10)	(11)
NGC 4570	159.3 ± 0.2	0.73 ± 0.03	158.5 ± 2.2	0.8	0.011 ± 0.004	162.4	N	N	RR/NF	e
NGC 4578	32.9 ± 1.4	0.29 ± 0.01	212.0 ± 4.0	0.9	0.024 ± 0.012	125.8	N	N	RR/NF	e
NGC 4596	119.8 ± 13.8	0.25 ± 0.02	125.0 ± 4.5	5.2	0.027 ± 0.014	89.2	B	N	RR/2m	e
NGC 4608	111.5 ± 44.9	0.07 ± 0.20	287.5 ± 8.8	4.0	0.050 ± 0.025	43.8	BR	N	RR/NF	e
NGC 4612	145.9 ± 6.4	0.32 ± 0.04	328.0 ± 8.5	2.1	0.037 ± 0.025	78.9	BR	N	RR/2m	e
NGC 4621	162.5 ± 3.6	0.32 ± 0.11	344.5 ± 2.2	2.0	0.020 ± 0.005	115.6	N	N	RR/NF	e
NGC 4623	175.5 ± 0.5	0.67 ± 0.04	175.0 ± 8.5	0.5	0.040 ± 0.027	77.9	N	N	RR/NF	e
NGC 4624	112.7 ± 9.7	0.06 ± 0.06	293.0 ± 5.0	0.3	0.045 ± 0.015	99.9	B	N	RR/NF	e
NGC 4636	144.2 ± 1.2	0.23 ± 0.06	267.0 ± 89.8	57.2	0.302 ± 0.224	9.8	N	N	NRR/LV	a
NGC 4638	121.2 ± 2.7	0.39 ± 0.04	124.5 ± 1.5	3.3	0.015 ± 0.006	154.6	N	N	RR/NF	e
NGC 4643	57.1 ± 39.0	0.12 ± 0.15	48.0 ± 4.2	9.1	0.030 ± 0.009	90.1	BR	N	RR/2m	e
NGC 4649	91.3 ± 3.6	0.16 ± 0.01	271.5 ± 3.8	0.2	0.033 ± 0.012	94.1	N	N	RR/NF	e
NGC 4660	96.9 ± 2.8	0.30 ± 0.12	277.5 ± 1.8	0.6	0.011 ± 0.004	147.9	N	N	RR/2m	e
NGC 4684	22.0 ± 0.7	0.63 ± 0.00	204.5 ± 5.0	2.5	0.027 ± 0.017	78.5	N	N	RR/NF	e
NGC 4690	151.7 ± 2.9	0.29 ± 0.03	331.0 ± 25.8	0.7	0.116 ± 0.068	26.8	N	N	NRR/NF	b
NGC 4694	142.5 ± 0.5	0.52 ± 0.08	324.5 ± 19.2	2.0	0.099 ± 0.088	27.1	N	FB	RR/NF	e
NGC 4697	67.2 ± 3.9	0.32 ± 0.04	247.5 ± 2.0	0.3	0.014 ± 0.006	111.4	N	N	RR/NF	e
NGC 4710	27.4 ± 0.2	0.75 ± 0.03	207.5 ± 3.8	0.1	0.028 ± 0.015	98.6	N	D	RR/NF	e
NGC 4733	114.1 ± 4.7	0.06 ± 0.00	337.5 ± 89.8	43.4	0.382 ± 0.287	6.3	B	N	NRR/LV	a
NGC 4753	85.4 ± 5.2	0.50 ± 0.03	88.5 ± 2.5	3.1	0.022 ± 0.008	148.7	I	F	RR/2m	e
NGC 4754	21.2 ± 0.3	0.48 ± 0.01	206.0 ± 3.0	4.8	0.018 ± 0.008	173.8	B	N	RR/NF	e
NGC 4762	29.6 ± 3.2	0.83 ± 0.10	30.0 ± 1.5	0.4	0.048 ± 0.011	136.7	N	N	RR/NF	e
NGC 4803	9.1 ± 1.7	0.37 ± 0.01	3.5 ± 22.2	5.6	0.118 ± 0.098	35.5	N	N	RR/2s	d
NGC 5103	140.6 ± 4.5	0.35 ± 0.09	318.5 ± 4.0	2.1	0.045 ± 0.019	103.3	N	N	RR/NF	e
NGC 5173	100.3 ± 1.4	0.13 ± 0.01	279.5 ± 16.8	0.8	0.042 ± 0.057	34.5	N	B	RR/NF	e
NGC 5198	14.7 ± 3.7	0.17 ± 0.02	46.5 ± 24.5	31.8	0.270 ± 0.077	25.9	N	N	NRR/NF	b
NGC 5273	8.9 ± 1.0	0.16 ± 0.02	190.5 ± 7.0	1.6	0.035 ± 0.024	65.0	N	N	RR/NF	e
NGC 5308	59.5 ± 0.5	0.80 ± 0.04	237.5 ± 2.2	2.0	0.012 ± 0.005	188.1	N	N	RR/2m	e
NGC 5322	91.8 ± 1.1	0.36 ± 0.03	273.0 ± 7.2	1.2	0.488 ± 0.172	73.3	N	N	NRR/CRC	c
NGC 5342	153.4 ± 0.6	0.54 ± 0.05	332.5 ± 2.5	0.9	0.031 ± 0.014	146.1	N	N	RR/NF	e
NGC 5353	140.4 ± 4.9	0.48 ± 0.04	322.0 ± 1.0	1.6	0.012 ± 0.005	244.3	B	D	RR/NF	e
NGC 5355	27.1 ± 11.7	0.32 ± 0.01	29.0 ± 14.0	1.9	0.056 ± 0.040	49.5	I	N	RR/NF	e
NGC 5358	139.5 ± 0.3	0.62 ± 0.01	318.0 ± 8.2	1.5	0.037 ± 0.022	85.2	N	N	RR/NF	e
NGC 5379	58.3 ± 2.2	0.66 ± 0.01	61.0 ± 10.0	2.7	0.029 ± 0.027	119.0	R	FBR	RR/NF	e
NGC 5422	152.3 ± 0.0	0.79 ± 0.03	334.0 ± 3.8	1.7	0.024 ± 0.009	160.9	N	D	RR/NF	e
NGC 5473	154.2 ± 0.9	0.21 ± 0.01	157.5 ± 3.2	3.3	0.037 ± 0.010	170.9	BR	N	RR/NF	e
NGC 5475	166.2 ± 1.9	0.70 ± 0.03	345.0 ± 2.5	1.2	0.021 ± 0.011	129.1	N	N	RR/NF	e
NGC 5481	110.0 ± 2.4	0.27 ± 0.07	241.0 ± 19.0	49.0	0.229 ± 0.136	48.9	N	N	NRR/KDC	c
NGC 5485	0.9 ± 3.6	0.26 ± 0.04	259.0 ± 6.8	78.1	0.084 ± 0.020	63.7	N	D	NRR/NF	b
NGC 5493	123.0 ± 31.1	0.20 ± 0.14	121.0 ± 1.0	2.0	0.010 ± 0.003	217.8	I	N	RR/NF	e
NGC 5500	128.4 ± 4.2	0.20 ± 0.04	129.0 ± 35.2	0.6	0.161 ± 0.088	24.9	N	N	NRR/NF	b
NGC 5507	60.3 ± 0.5	0.47 ± 0.02	60.5 ± 3.5	0.2	0.027 ± 0.009	164.1	N	N	RR/2m	e
NGC 5557	82.6 ± 3.8	0.16 ± 0.04	336.0 ± 4.5	73.4	0.206 ± 0.102	20.5	S	N	NRR/NF	b
NGC 5574	62.7 ± 15.0	0.48 ± 0.04	247.5 ± 11.8	4.8	0.043 ± 0.030	50.0	I	N	RR/NF	e
NGC 5576	89.6 ± 2.6	0.31 ± 0.02	277.0 ± 16.5	7.4	0.133 ± 0.045	30.3	N	N	NRR/NF	b
NGC 5582	28.8 ± 1.7	0.35 ± 0.05	29.5 ± 2.8	0.7	0.012 ± 0.009	135.5	R	N	RR/NF	e
NGC 5611	64.6 ± 2.0	0.55 ± 0.09	244.0 ± 3.0	0.6	0.009 ± 0.008	139.2	N	N	RR/NF	e
NGC 5631	137.7 ± 64.8	0.07 ± 0.02	119.0 ± 8.8	18.7	0.323 ± 0.165	58.9	N	D	NRR/KDC	c
NGC 5638	153.2 ± 8.1	0.10 ± 0.04	140.0 ± 6.8	13.2	0.055 ± 0.025	82.3	N	N	RR/NF	e
NGC 5687	102.0 ± 0.9	0.37 ± 0.05	284.0 ± 3.8	2.0	0.029 ± 0.011	125.1	N	N	RR/NF	e
NGC 5770	34.8 ± 36.6	0.06 ± 0.09	42.0 ± 14.2	7.2	0.071 ± 0.056	47.6	BR	N	RR/NF	e
NGC 5813	133.2 ± 2.0	0.27 ± 0.03	152.5 ± 8.0	19.3	0.225 ± 0.071	91.6	N	N	NRR/KDC	c
NGC 5831	131.1 ± 4.8	0.10 ± 0.02	110.5 ± 22.5	20.6	0.299 ± 0.144	30.1	N	N	NRR/KDC	c
NGC 5838	40.1 ± 1.2	0.62 ± 0.06	39.5 ± 1.5	0.6	0.012 ± 0.004	212.9	B	N	RR/NF	e
NGC 5839	101.2 ± 14.3	0.12 ± 0.04	278.0 ± 6.0	3.2	0.026 ± 0.016	93.9	BR	N	RR/NF	e
NGC 5845	138.3 ± 13.1	0.31 ± 0.09	321.0 ± 3.5	2.7	0.023 ± 0.005	126.8	N	N	RR/2m	e
NGC 5846	53.3 ± 1.9	0.08 ± 0.03	312.5 ± 34.5	79.2	0.269 ± 0.122	10.9	N	N	NRR/LV	a
NGC 5854	54.8 ± 0.1	0.68 ± 0.01	51.5 ± 3.8	3.3	0.026 ± 0.015	122.9	BR	N	RR/NF	e

Table D1 – *continued*

Name	PA$_{phot}$ (°)	ϵ	PA$_{kin}$ (°)	Ψ (°)	$\overline{k_5/k_1}$	k_1^{max} (km s^{-1})	Morphological property	Dust feature	Kinematic structure	Group
(1)	(2)	(3)	(4)	(5)	(6)	(7)	(8)	(9)	(10)	(11)
NGC 5864	65.6 ± 0.5	0.68 ± 0.02	75.0 ± 5.2	9.4	0.037 ± 0.016	133.6	B	N	RR/NF	e
NGC 5866	125.0 ± 1.1	0.58 ± 0.08	126.5 ± 1.2	1.5	−1.000 ± −1.000	157.4	N	D	RR/NF	e
NGC 5869	115.8 ± 4.2	0.32 ± 0.07	113.5 ± 4.5	2.3	0.023 ± 0.012	105.8	S	N	RR/NF	e
NGC 6010	102.9 ± 0.1	0.75 ± 0.05	104.5 ± 3.5	1.6	0.032 ± 0.011	136.9	N	N	RR/NF	e
NGC 6014	156.6 ± 91.9	0.12 ± 0.02	147.0 ± 8.5	9.6	0.033 ± 0.028	89.9	N	DBR	RR/NF	e
NGC 6017	137.5 ± 54.5	0.11 ± 0.08	132.5 ± 6.5	3.2	0.047 ± 0.016	89.1	N	D	RR/NF	e
NGC 6149	18.0 ± 1.0	0.32 ± 0.01	201.0 ± 4.2	3.0	0.018 ± 0.014	85.0	N	N	RR/NF	e
NGC 6278	125.8 ± 1.3	0.45 ± 0.05	305.5 ± 4.8	0.3	0.024 ± 0.010	189.8	N	N	RR/NF	e
NGC 6547	131.4 ± 1.6	0.67 ± 0.02	131.5 ± 1.5	0.1	0.024 ± 0.008	159.7	N	N	RR/NF	e
NGC 6548	67.8 ± 53.9	0.11 ± 0.18	66.5 ± 3.2	1.3	−1.000 ± −1.000	213.9	B	N	RR/NF	e
NGC 6703	69.0 ± 21.6	0.03 ± 0.01	181.5 ± 88.2	67.5	0.511 ± 0.232	9.2	N	N	NRR/LV	a
NGC 6798	141.2 ± 2.9	0.47 ± 0.03	139.0 ± 6.8	2.2	0.044 ± 0.018	112.5	N	N	RR/2m	e
NGC 7280	74.2 ± 0.3	0.36 ± 0.01	260.0 ± 5.5	5.8	0.027 ± 0.016	97.8	B	N	RR/2m	e
NGC 7332	155.2 ± 0.9	0.74 ± 0.04	152.5 ± 4.0	2.7	0.033 ± 0.012	93.2	N	N	RR/NF	e
NGC 7454	145.8 ± 1.2	0.26 ± 0.06	324.5 ± 40.0	1.3	0.204 ± 0.126	25.1	N	N	NRR/NF	b
NGC 7457	124.8 ± 0.7	0.47 ± 0.00	304.0 ± 6.8	0.8	0.040 ± 0.031	72.8	N	N	RR/NF	e
NGC 7465	155.0 ± 1.1	0.33 ± 0.02	166.5 ± 29.0	11.5	0.125 ± 0.044	62.8	I	F	NRR/KDC	c
NGC 7693	154.0 ± 3.5	0.24 ± 0.02	338.0 ± 13.0	4.0	0.052 ± 0.040	62.6	B	N	RR/NF	e
NGC 7710	133.7 ± 0.1	0.59 ± 0.08	134.0 ± 41.5	0.3	0.055 ± 0.062	50.8	N	N	RR/2s	d
PGC 016060	156.7 ± 0.9	0.72 ± 0.04	159.0 ± 2.0	2.3	0.016 ± 0.015	128.4	N	N	RR/NF	e
PGC 028887	32.2 ± 1.0	0.33 ± 0.02	212.0 ± 9.5	0.2	0.279 ± 0.121	75.3	N	N	NRR/KDC	c
PGC 029321	47.8 ± 6.2	0.12 ± 0.01	56.5 ± 37.0	8.7	0.059 ± 0.039	39.8	N	F	RR/NF	e
PGC 035754	78.9 ± 3.2	0.33 ± 0.02	86.0 ± 11.0	7.1	0.055 ± 0.041	54.5	N	N	RR/NF	e
PGC 042549	64.7 ± 0.9	0.39 ± 0.01	241.0 ± 6.0	3.7	0.035 ± 0.019	117.1	B	N	RR/NF	e
PGC 044433	14.4 ± 0.4	0.64 ± 0.03	195.5 ± 4.2	1.1	0.022 ± 0.022	62.6	N	N	RR/NF	e
PGC 050395	10.5 ± 0.9	0.27 ± 0.03	185.5 ± 40.5	5.0	0.195 ± 0.151	16.5	N	N	NRR/CRC	c
PGC 051753	33.6 ± 0.2	0.51 ± 0.03	215.5 ± 8.8	1.9	0.026 ± 0.022	86.7	N	N	RR/NF	e
PGC 054452	105.4 ± 9.6	0.16 ± 0.03	278.5 ± 16.5	6.9	0.044 ± 0.033	46.1	R	N	RR/NF	e
PGC 056772	9.9 ± 1.7	0.45 ± 0.02	191.0 ± 5.5	1.1	0.037 ± 0.025	69.5	N	D	RR/2s	d
PGC 058114†	80.7 ± 19.0	0.20 ± 0.09	247.0 ± 10.0	13.7	−1.000 ± −1.000	44.1	U	U	U	f
PGC 061468	102.5 ± 8.7	0.28 ± 0.06	105.0 ± 11.5	2.5	0.044 ± 0.035	59.4	N	N	RR/NF	e
PGC 071531†	83.2 ± 4.0	0.29 ± 0.06	264.5 ± 21.8	1.3	0.038 ± 0.038	49.9	U	U	RR/NF	e
PGC 170172	18.5 ± 4.2	0.09 ± 0.00	18.0 ± 89.8	0.5	−1.000 ± −1.000	39.7	B	N	U	f
UGC 03960	44.1 ± 1.6	0.28 ± 0.02	227.5 ± 89.8	3.4	0.350 ± 0.259	21.6	N	N	NRR/NF	b
UGC 04551	113.2 ± 0.3	0.61 ± 0.01	113.5 ± 5.5	0.3	0.031 ± 0.014	78.3	R	N	RR/NF	e
UGC 05408	153.0 ± 5.4	0.12 ± 0.01	150.0 ± 17.0	3.0	0.056 ± 0.080	42.1	B	FB	RR/NF	e
UGC 06062	23.6 ± 3.9	0.45 ± 0.05	32.5 ± 5.5	8.9	0.042 ± 0.015	114.8	B	N	RR/NF	e
UGC 06176	24.1 ± 0.3	0.49 ± 0.02	200.5 ± 6.5	3.6	0.021 ± 0.017	116.1	BR	FBR	RR/NF	e
UGC 08876	24.0 ± 0.2	0.63 ± 0.04	204.5 ± 7.2	0.5	0.030 ± 0.023	60.9	R	N	RR/NF	e
UGC 09519	76.4 ± 2.9	0.25 ± 0.08	249.5 ± 4.2	6.9	0.025 ± 0.016	90.4	N	F	RR/NF	e

Notes. Column (1): the name is the principal designation from the LEDA, which is used as the standard designation; column (2): global photometric PA and the uncertainty in degrees, measured east of north and within 2.5–3 half-light radii; column (3): global ellipticity and uncertainty, measured within 2.5–3 half-light radii; column (4): global kinematic PA and the uncertainty in degrees, measured east of north at the receding part of the velocity map; column (5): kinematic misalignment angle in degrees. In the text, the uncertainty values for the global kinematic angle are assigned to the kinematic misalignment angle; column (6): luminosity-weighted average ratio of the harmonic terms obtained by KINEMETRY; column (7): maximal rotational velocity reached within the SAURON FoV; column (8): morphological properties of galaxies – B: bar, R: ring, BR: bar and ring, S: shells, I: other interaction feature and U: unknown; column (9): dust features – D: dusty disc, F: dusty filament, B: blue nucleus and BR: blue ring. Combinations of these are possible; column (10): kinematic structure (see Table 2 for a detailed explanation of all classes); and column (11): kinematic group – a: LV galaxies, b: NRR galaxies, c: KDC and CRC galaxies, d: 2σ peak galaxies, e: all other RR galaxies and f: unclassified galaxies.

The value of −1.0 in columns (5) and (6) is given to galaxies for which the KINEMETRY analysis was not successful. The two galaxies with † did not have SDSS or INT data and we used 2MASS *K*-band images to determine PA$_{phot}$ and ϵ. This table is also available at our project website: http://purl.org/atlas3d

This paper has been typeset from a TEX/LATEX file prepared by the author.